DNA tensiometer reveals catch-bond detachment kinetics of kinesin-1, -2 and -3

Crystal R. Noell[1], Tzu-Chen Ma[1], Rui Jiang[1], Scott A. McKinley[2], William O. Hancock*[1,3]

[1] Department of Biomedical Engineering, Pennsylvania State University, University Park, Pennsylvania, USA
[2] Department of Mathematics, Tulane University, New Orleans, Louisiana, USA
[3] Department of Chemistry, Pennsylvania State University, University Park, Pennsylvania, USA

* Corresponding author
Email: woh1@psu.edu

Author Contributions: S.A.M. and W.O.H. conceived of original idea, C.R.N., R.J. and W.O.H. designed research; C.R.N., R.J. and T.M. performed research; C.R.N., T.M. and S.A.M. analyzed data; C.R.N., T.M., S.A.M., and W.O.H. wrote the paper.
Competing Interest Statement: The authors declare that they have no known competing financial interests or personal relationships that could have appeared to influence the work reported in this paper.
Classification: Biological Sciences; Biophysics and Computational Biology
Keywords: Kinesin, intracellular transport, molecular mechanics, molecular machine, mechanochemistry

Abstract

Bidirectional cargo transport by kinesin and dynein is essential for cell viability and defects are linked to neurodegenerative diseases. Computational modeling suggests that the load-dependent off-rate is the strongest determinant of which motor 'wins' a kinesin-dynein tug-of-war, and optical tweezer experiments find that the load-dependent detachment sensitivity of transport kinesins is kinesin-3 > kinesin-2 > kinesin-1. However, in reconstituted kinesin-dynein pairs vitro, all three kinesin families compete nearly equally well against dynein. Modeling and experiments have confirmed that vertical forces inherent to the large trapping beads enhance kinesin-1 dissociation rates. In vivo, vertical forces are expected to range from negligible to dominant, depending on cargo and microtubule geometries. To investigate the detachment and reattachment kinetics of kinesin-1, 2 and 3 motors against loads oriented parallel to the microtubule, we created a DNA tensiometer comprising a DNA entropic spring attached to the microtubule on one end and a motor on the other. Kinesin dissociation rates at stall were slower than detachment rates during unloaded runs, and the complex reattachment kinetics were consistent with a weakly-bound 'slip' state preceding detachment. Kinesin-3 behaviors under load suggested that long KIF1A run lengths result from the concatenation of multiple short runs connected by diffusive episodes. Stochastic simulations were able to recapitulate the load-dependent detachment and reattachment kinetics for all three motors and provide direct comparison of key transition rates between families. These results provide insight into how kinesin-1, -2 and -3 families transport cargo in complex cellular geometries and compete against dynein during bidirectional transport.

Significance Statement

Kinesin and dynein motor proteins transport intracellular cargo bidirectionally along microtubule tracks, with the speed and directionality of transport involving competition between motor teams. We created a 'DNA tensiometer' that uses DNA as a spring to measure kinesin performance against loads oriented parallel to the microtubule. We find that dissociation rates for all three families of transport kinesins slow down with imposed loads. Dyneins are also thought to possess this 'catch-bond' behavior, meaning that both motors will hang on tightly during a tug-of-war. Building on previous work that showed combined vertical and horizontal loads cause faster detachment rates under load, we conclude that the effectiveness of kinesins during bidirectional transport depends strongly on the geometry of their cargo.

Introduction

Bidirectional cargo transport by kinesin and dynein motors is essential for cell viability, and disruptions in transport are linked to neurological diseases including hereditary spastic paraplegia, microcephaly and amyotrophic lateral sclerosis (Brenner et al., 2018; Caballero Oteyza et al., 2014; Makrythanasis et al., 2018; Millecamps & Julien, 2013; Moawia et al., 2017; Pant et al., 2022; Reid et al., 2002; Zhou et al., 2024). It has been established that kinesin and dynein, which move in opposite directions along microtubules, are often bound simultaneously to the same cargo (Encalada et al., 2011; Hendricks et al., 2010; Soppina et al., 2009; Welte, 2004). This has led to the 'tug-of-war' model, in which the direction of cargo movement is determined by which team of motors dominates (Belyy et al., 2016; Gross, 2004; Hancock, 2014; Hendricks et al., 2010; Muller et al., 2008). How well motors compete is determined by the size of the team, their load-dependent motor properties, and multiple regulation mechanisms, many of which are still emerging (Cason & Holzbaur, 2022; D'Souza et al., 2024; Hancock, 2014; Reck-Peterson et al., 2018; Yildiz, 2025). Furthermore, the large range of cargo sizes and the complexity of microtubule organization in cells means that motors generate and are subjected to forces both parallel and perpendicular to their microtubule track.

Intuitively, a motor's effectiveness in transporting cargo rests on its ability to remain bound to its microtubule track. Consistent with this, computational simulations have found that the load-dependent off-rate of a motor is the most important determinant of how well a kinesin competes against dynein in bidirectional transport (Ma et al., 2023; Ohashi et al., 2019). Simply put, motors that remain attached under load beat motors that readily detach under load. Single-bead optical tweezers have found that the transport motors kinesin-1, -2, and -3 all act as slip bonds, defined as load accelerating their detachment rate. Their propensity to detach under load varies strongly by family, with relative load sensitivity kinesin-3 > kinesin-2 > kinesin-1 (Andreasson et al., 2015; Budaitis et al., 2021; Pyrpassopoulos et al., 2023; Tomishige et al., 2002). Based on this behavior, it was surprising that when kinesin-1 was linked to dynein, the complex moved at near-zero speeds for up to tens of seconds, much longer than predicted based on previously measured kinesin-1 off-rates (Andreasson et al., 2015; Feng et al., 2020; Yildiz et al., 2008). Moreover, kinesin-1, -2, and -3 all fared equally well against dynein, contrary to the differing load-dependent detachment rates measured in single-bead optical tweezer experiments (Gicking et al., 2022).

Recent work suggests a solution to this paradox, namely that the ~micron scale beads used for optical trapping result in significant forces oriented perpendicular to the microtubule as the motor pulls against the force of the trap. First, the load-dependent dissociation rate from single-bead optical trapping was accounted for by a model in which the effects of horizontal loads on detachment is highly asymmetric and vertical loads play a dominant role in detachment, particularly against hindering loads (Khataee & Howard, 2019). Second, when a three-bead optical trapping geometry was used (in which the motor is raised up on a pedestal bead and the microtubule was held by beads attached to either end of the microtubule) motors remained bound longer than in the single-bead geometry (Pyrpassopoulos et al., 2023; Pyrpassopoulos et al., 2020). Third, when kinesin-1 motors were connected to a microtubule by a micron-long segment of DNA, very long residence times were observed, consistent with catch-bond behavior

(Kuo et al., 2022). In cells, kinesin and dynein transport cargoes that range from tens of nm in diameter (like vesicles), where motor forces are expected to be aligned parallel to the microtubule, up to several microns (like mitochondria and nuclei), where vertical forces are expected to be much larger. Thus, understanding the influence of vertical and horizontal forces on transport motors is important for understanding the mechanics underlying bidirectional transport in cells.

The goal of the present study was to characterize the load-dependent detachment kinetics of kinesin-1, -2 and -3 motors in a geometry that eliminates vertical forces inherent in traditional optical trapping studies. Building on previous approaches, we used double stranded DNA (dsDNA), which acts as an entropic spring to resist the pN-level forces generated by the motors (Diez et al., 2003; Iwaki et al., 2016; Kuo et al., 2022; Marko & Siggia, 1995; Shukla et al., 2022; Urbanska et al., 2021). We found that kinesin-1, -2, and -3 all remained at stall for multiple seconds before releasing, which is substantially longer than the unloaded run times for kinesin-1 and -2. This behavior of slower off-rates under load is defined as a 'catch bond' and contrasts with the normal 'slip bond' behavior load-accelerated off-rates seen previously for kinesin (Thomas et al., 2008). Following the termination of a stall, motors reengaged with the microtubule with complex kinetics that were consistent with a 'slip' state that preceded full detachment. To compare the key transition rates that determined the family-specific motor behaviors, we developed a stochastic model that was able to recapitulate the experimental results for all three motors.

Results

Constructing a motor-bound DNA tensiometer

To study motor performance against a resistive load oriented parallel to the microtubule, we constructed a DNA tensiometer consisting of a ~ 1 μm strand of dsDNA attached to the microtubule on one end and a motor on the other (Figure 1A). We used TIRF microscopy to visualize the motor moving against the entropic elasticity of the DNA spring. Due to the nonlinear elasticity of the DNA (Figure 1B) (Iwaki et al., 2016; Marko & Siggia, 1995), the motor moves under minimal load until it stretches the DNA to near its contour length, at which point it stalls (Figure 1C-E).

Our DNA-motor tensiometer consists of a 3,009 bp (999 nm contour length) dsDNA 'spring' that was synthesized by PCR using a biotinylated forward primer for attachment to the microtubule and a reverse primer containing a 3' overhang for motor attachment (details in Methods). We investigated members of the three dominant families of kinesin transport motors, kinesin-1 (*Drosophila melanogaster* KHC), kinesin-2 (*Mus musculus* Kif3A), and kinesin-3 (*Rattus norvegicus* Kif1A) used in our previous kinesin-dynein study (Gicking et al., 2022). In each case, the motor and neck linker domains were fused to the stable neck-coil domain (residues 345-406) of kinesin-1, followed by EGFP, a SNAP tag, and His_6 tag, as described previously (Gicking et al., 2022). This dimerization strategy avoids any autoinhibition and enables the most direct comparison of the motor properties between these three families. Motors were conjugated to an oligonucleotide complimentary to the 3' overhang of the dsDNA spring via their C-terminal SNAP tag. The DNA tensiometer complex (ure 1A) was created in a flow cell by sequentially flowing in biotinylated microtubules, neutravidin, biotinylated

dsDNA, and Qdot-functionalized motors containing the complimentary oligo (described fully in Methods).

The resulting dsDNA tensiometer kymographs (Figure 1C) show a reproducible behavior of moving, stalling, and returning to origin multiple times, which contrasts with the singular attachment, unidirectional movement and detachment of motors not bound by DNA (Figure S1). Because motors are tethered to the microtubule by the flexible DNA, large fluctuations around the origin are observed when the motor is detached (Figure 1C-H). Consistent with these fluctuations, initial attachment points were variable and roughly normally distributed with a standard deviation of 145 nm (Figure S2). Upon engagement with the microtubule, the motor walks at a steady velocity, consistent with the expected nonlinear stiffness of the dsDNA tether (Figure 1B), until it either disengages and returns to origin or reaches a stall state. Stalls are terminated either by the motor slipping backwards a short distance and restarting a new ramp, or by the motor fully disengaging and returning to the baseline (Figure 1E-H and Figure S3). To confirm that motors are indeed extending the DNA and that Qdots are not enabling multi-motor assemblies, we incorporated Cy5-dCTP into the dsDNA and left the Qdots out of the reaction. In this case, clear extensions of the DNA spring could be observed, and the stall durations were of similar duration (Figure S4). In all subsequent experiments dsDNA was labeled with a low concentration of Cy5-dCTP to confirm colocalization of the DNA and the microtubule before collecting tensiometer data.

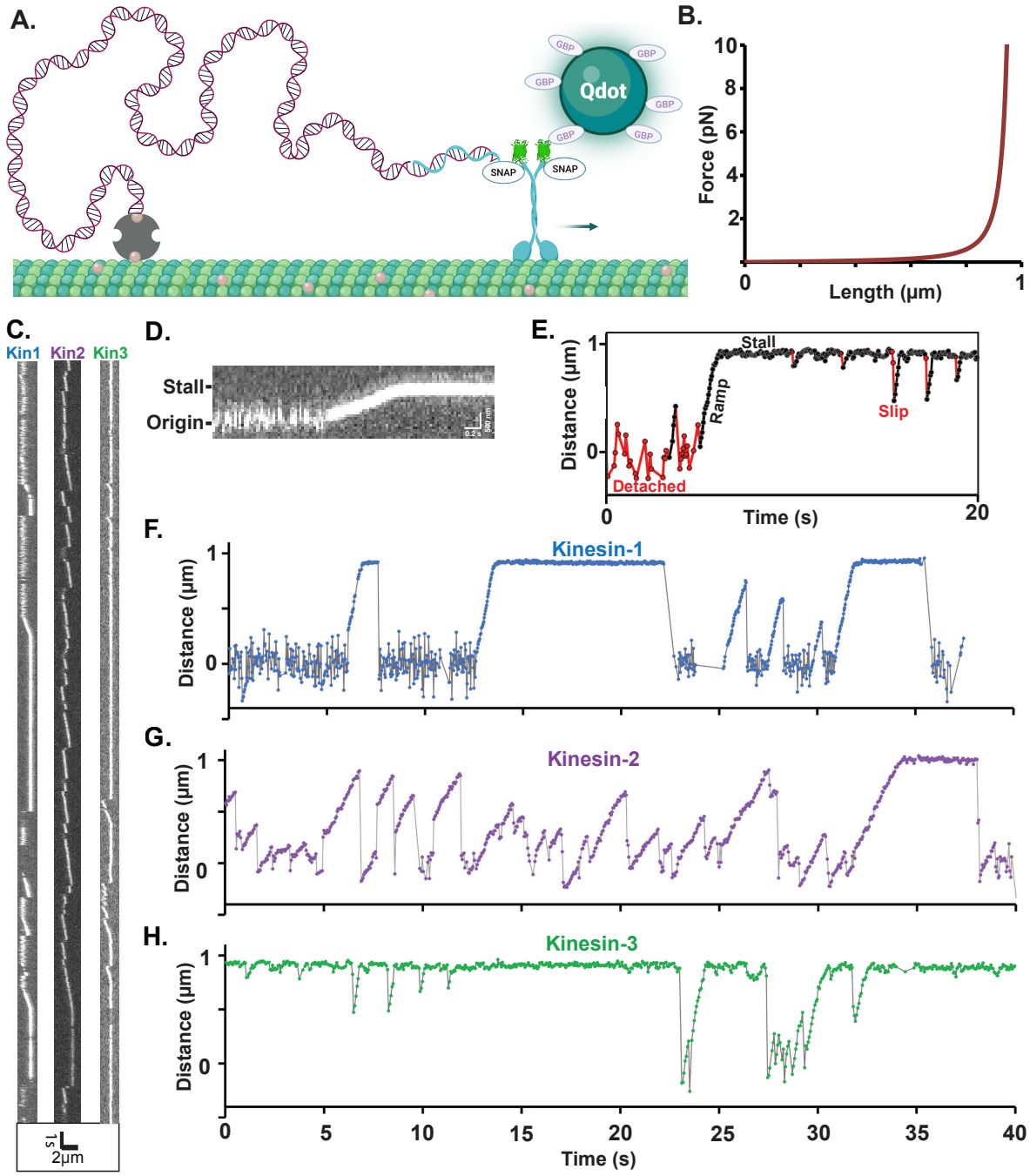

Figure 1. Experimental Design and Raw Data from Motor-DNA Tensiometers. (A) Schematic of a motor-DNA tensiometer, consisting of a dsDNA (burgundy) connected on one end to a kinesin motor through a complimentary oligo (blue), and on the other end to the MT using biotin-avidin (tan and gray, respectively). A Qdot functionalized with GFP binding protein nanobodies is attached to the motor's GFP tag and used to track motor position. (Not to scale; motor and Qdot are both ~20 nm and DNA is ~1 micron) (B) Predicted force extension curve for a worm-like chain 3009 bp dsDNA based on a 50 nm persistence length. (C) Representative kymographs of motor-DNA tensiometers for kinesins-1, -2 and -3. (D) Enlarged kymograph showing diffusion around the origin, ramp, and stall. (E) Example distance vs. time trace (kinesin-3), highlighting detached durations (red), ramps and stalls (black) where the motor has

pulled the DNA taut, and transient slips during stall (red). (F-H) Representative distance vs. time plots for kinesin-1 (F), kinesin-2 (G) and kinesin-3 (H), corresponding to the kymographs in (C). Further examples are shown in Figure S3.

Kinesin-1 and -2 act as catch-bonds at stall

The first question we addressed was: what are the detachment rates of kinesin-1, -2 and -3 motors at stall? The load-dependence of protein-protein interactions can be described as a slip-bond (Bell, 1978), defined as a faster off-rate under load; an ideal bond, defined as an off-rate that is independent of load; or a catch-bond, in which the off-rate is slower under load (Thomas et al., 2008). Single-bead optical trapping studies consistently find slip-bond characteristics for kinesin-1, 2 and 3 (Andreasson et al., 2015; Budaitis et al., 2021; Rao & Gennerich, 2022), whereas dynein off-rates have been described as a slip-bond or catch-bond (Ezber et al., 2020; Kunwar et al., 2011; Rai et al., 2013; Sanghavi et al., 2021; Soppina et al., 2009).

We define stall duration as the time that a motor stalls against the hindering load of fully extended DNA, without further detectable stepping. Stalls are terminated by the motor detectably (>60 nm) slipping backwards or by disengaging and returning to the origin (Figure 1E). Although we don't directly measure the stall force, based on the predicted force-extension curve of the dsDNA (Figure 1B), the displacements are consistent with the 4-6 pN stall forces for kinesin-1, -2 and -3 measured using optical traps (Blehm et al., 2013; Budaitis et al., 2021; Kojima et al., 1997; Schroeder et al., 2012; Svoboda & Block, 1994; Visscher et al., 1999). Stall durations were compared to the unloaded single-motor run durations determined from TIRF kymograph analysis (Figure S1).

To compare unloaded to stall off-rates, cumulative distributions of the run and stall durations were plotted for each motor and fit with a single exponential function (Figure 2). The kinesin-1 tensiometer stall duration time constant was 3.01 s, with 95% confidence intervals (CI) of 2.30 to 3.79 s determined via bootstrapping in MEMLET with 1000 iterations) (Woody et al., 2016) (N= 78 stalls). In contrast, the kinesin-1 unloaded run duration time constant, measured by a traditional TIRF assay, was 1.04 s, (95% CI of 0.79 to 1.30 s; N= 59) (Figure 2A). Stall durations longer than unloaded run durations indicate that load slows the off-rate, the definition of a catch-bond (Thomas et al., 2008). Similarly, the kinesin-2 tensiometer stall duration time constant of 2.83 s (95% CI of 2.03 to 3.79 s; N= 50) was longer than its unloaded run duration of 1.07 s (95% CI of 0.85 to 1.35 s; N= 87), also indicating a catch-bond. Conversely, the kinesin-3 tensiometer stall duration time constant of 1.89 s (95% CI of 1.53 to 2.31 s; N= 140) was shorter than its unloaded run duration of 2.74 s (95% CI of 2.33 to 3.17 s; N= 106), indicating a slip-bond characteristic by this definition.

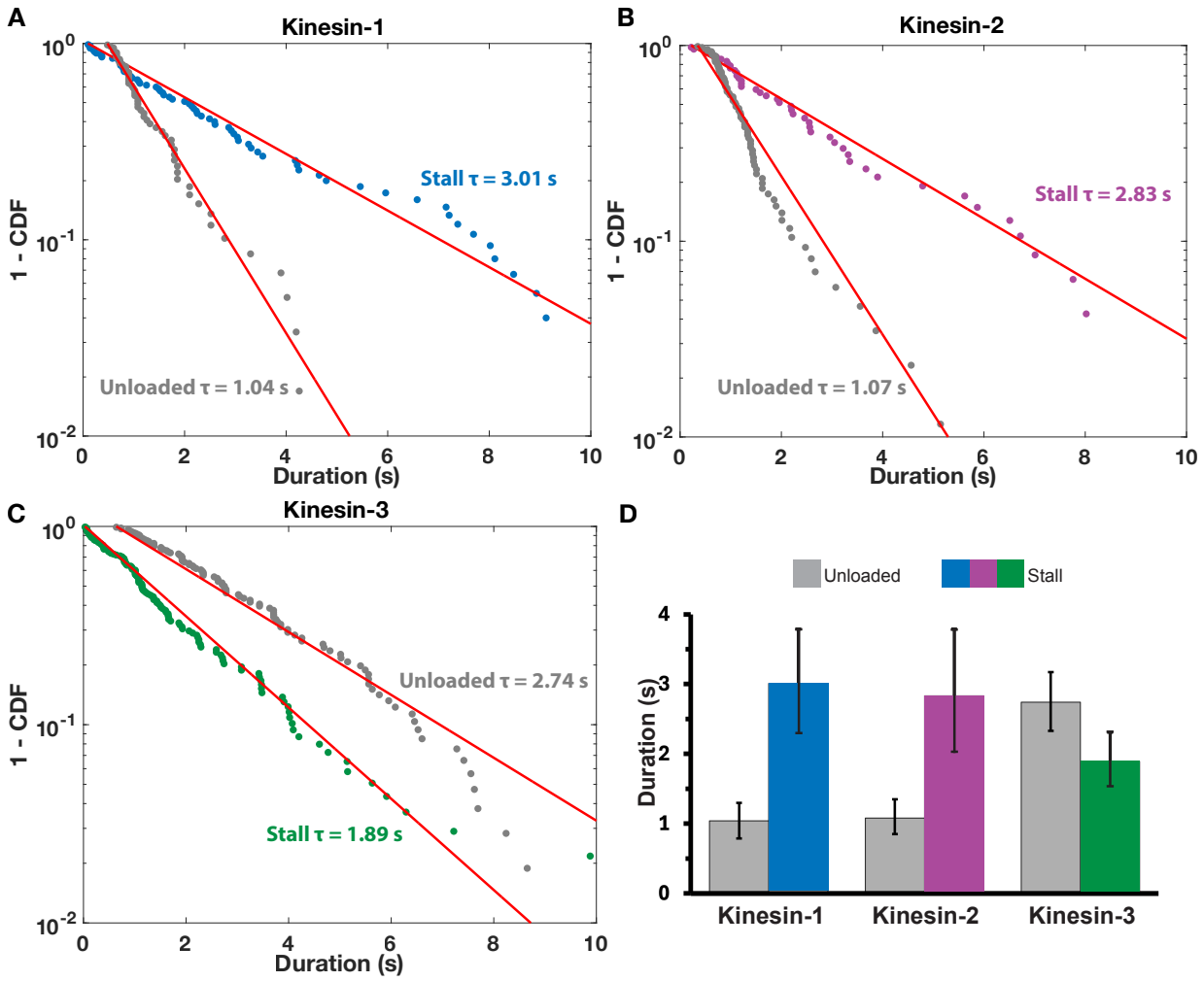

Figure 2. Tensiometer Stall Durations Indicate Catch-bond Behavior for Kinesin-1 and -2. Tensiometer stall durations are plotted for A) kinesin-1 (blue), (B) kinesin-2 (purple), and (C) kinesin-3 (green). Unloaded run durations for each motor are plotted in gray. Distributions were fit with a single exponential function using MEMLET to generate time constants, representing the mean durations. (D) Comparison of unloaded and stall durations for the three motors, with error bars indicating 95% CI. Stall durations >20s were excluded from the fit (three events for kinesin-1 and two events for kinesin-2). Bi-exponential fits of all data including >20 s are shown in Figure S5.

Kinesin-3 detaches readily under low load

To determine whether sub-stall hindering loads affect motor detachment rates, we compared tensiometer ramp durations to the tensiometer stall and unloaded run durations (Figure 3). We defined ramp durations as the time the motor spends walking against the DNA spring before a slip or detachment, or before reaching stall. Although the dsDNA force-extension curve (Figure 1B) predicts negligible loads until the DNA is close to fully extended, there are still non-zero loads imposed during the ramp phase that may affect motor detachment. Based on 10-20% slower ramp velocities relative to unloaded velocities for each motor, we estimated the apparent force to be ~1 pN (Table S1). To estimate the true detachment rate during the ramp phase in a way that takes into account both the successful and failed ramps, we used a Markov process model, coupled with Bayesian inference methods (detailed in Supplementary Material). In this

model, each increment of time is considered to be an independent opportunity to detach while assuming a constant detachment rate. Using the notation τ for the duration parameter, the probability of staying attached to the microtubule through a segment of duration Δ is $e^{-\Delta/\tau}$. Using this method, ramp duration parameters, τ, were calculated for each motor, along with 95% credible regions. Finally, to allow for proper comparison, we performed a similar analysis to obtain the stall and unloaded duration parameters along with their 95% credible regions (Figure 3). The stall and unloaded durations were similar to estimates from curve fitting in Figure 2 (Table S2).

The simplest prediction is that against the low loads experienced during ramps, the detachment rate should match the unloaded detachment rate. This was the case for kinesin-2, where the ramp duration of 0.97 s was within 95% CI of the unloaded run duration of 1.08 s (Figure 3B, Table S2). In contrast, the kinesin-1 ramp duration of 2.49 s was much closer to the stall duration (3.05 s) than the unloaded run duration (1.05 s) (Figure 3A). To test whether the ramp duration was affected by the DNA tether, we carried out a control experiment in which the DNA tether was linked to the kinesin-1 motor but not the microtubule. The run duration in that case was 1.40 s, slightly longer than the motor alone, but less than the kinesin-1 ramp duration (Figure S6). One possibility explanation for the longer kinesin-1 ramp is that the catch-bond character of kinesin-1 engages at low loads rather than rising proportionally to load or engaging only near stall.

The most notable ramp behavior was seen in kinesin-3, where the ramp duration of 0.75 s was nearly four-fold shorter than the unloaded run duration (2.76 s) and was more than two-fold shorter than the stall duration (1.90 s) (Figure 3C). As expanded on in the Discussion, the positively charged ‘K-loop’ in the kinesin-3 motor KIF1A is known to interact electrostatically with the negatively charged C-terminal tail of tubulin (Soppina et al., 2022; Zaniewski et al., 2020; Zaniewski & Hancock, 2023); thus, it is reasonable that even the low loads imposed during ramps are sufficient to overcome these weak electrostatic interactions. The ramp duration is arguably the best definition of the time before KIF1A motors enter a partially dissociated ‘slip’ state, meaning that the observed unloaded durations represent a concatenation of multiple shorter runs interspersed by short diffusive events. Notably, by defining the ramp duration as the motor’s behavior under low load, kinesin-3 can be classified as a catch bond because high load (stall) durations are longer than low load (ramp) durations.

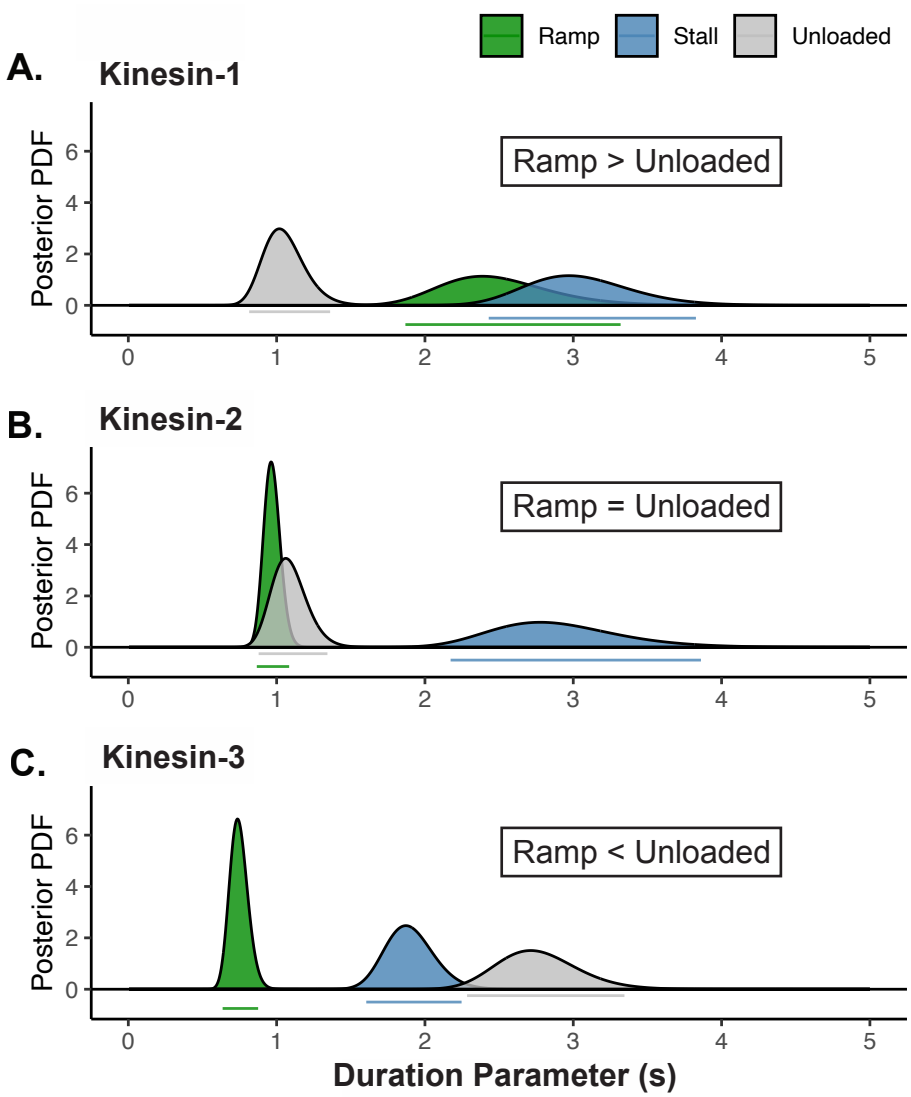

Figure 3. During Ramps, Kinesin-3 Detaches More Readily Than Under Zero Load. Unloaded, ramp, and stall duration parameters were estimated using a Markov process model, coupled with Bayesian inference methods. Curves show the posterior probability distributions of the duration parameters for (A) kinesin-1, (B) kinesin-2 and (C) kinesin-3. Bars below each peak indicate the 95% credible regions for the ramp (green), unloaded (gray) and stall (blue) duration parameters. Notably, the estimated ramp durations are larger, the same, and smaller than the unloaded run durations for kinesin-1, -2, and -3, respectively. For the unloaded and stall durations, this estimation method produces almost identical values as the maximum likelihood estimates in Figure 2 (values provided in Table S2).

Motor reengagement kinetics vary between families

Stall plateaus were terminated by three types of events: 1) small slips that initiated a new ramp, typically within a single frame (~40 ms), 2) the motor returning to the baseline and reengaging rapidly within a few frames (~100 msec), or 3) the motor returning to the baseline for a few seconds before reengaging (Figure 4A). We defined a slip event as a displacement of >60 nm from the plateau (distinguishable from normal small fluctuations at stall; Figure 1E) that recovers before reaching within 400 nm of the baseline (outside the range of normal baseline fluctuations; Figure 1F and S2). These

slip events have been observed previously for all three motor families in optical trapping experiments and are proposed to represent an intermediate state in which the motor exits the normal stepping cycle but remains associated with the microtubule (Jannasch et al., 2013; Pyrpassopoulos et al., 2023; Siddiqui et al., 2022; Sudhakar et al., 2021; Toleikis et al., 2020). As an initial analysis, we quantified the fraction of events for each motor (Figure 4A) and found that kinesin-3 had the highest proportion of slip events while kinesin-2 had the lowest proportion. In the context of pulling a large cargo through the viscous cytoplasm or competing against dynein in a tug-of-war, these slip events enable the motor to maintain force generation and, hence are distinct from true detachment events. Thus, we reanalyzed the stall durations for the three motors where slips are not counted and only disengagements where the motor returns to the baseline are counted as stall termination events (Figure 4B & C, Figure S7). By this definition, stall durations were between 1.5 and 3-fold longer for each motor. Notably, the kinesin-3 stall duration in this analysis was longer than its unloaded run duration, defining it as a catch-bond by this measure.

To obtain a more complete picture of the motor reengagement kinetics for each motor, we plotted the time before starting a new plateau ($t_{restarting}$), including all slips and reattachments (Figure 4D-F). In each case, the distributions included a fast phase and a long tail of slower events. The distributions were fit with a tri-exponential function with the fast phase (30, 130 and 40 msec, respectively) accounting for roughly half of the events (Figure 4 D-F, Table S3). The fast population corresponds to slip and fast reattachment events classified in Figure 4A. The slower phases, which represent detachment events where the motor fluctuated around the baseline before initiating a new ramp, were the fastest for kinesin-3 (time constants of 0.15 and 1.34 s) and the slowest for kinesin-1 (time constants of 1.51 and 20.9 s). Interestingly, the order of the reattachment kinetics (kinesin-3 > kinesin-2 > kinesin-1) and the ~10-fold ratio of kinesin-3 to kinesin-1 match published bimolecular on-rate constants for microtubule binding from stopped-flow experiments (1.1, 4.6, and 17 μM-1 s-1 for kinesin-1,-2 and -3, respectively (Chen et al., 2015; Feng et al., 2018; Zaniewski et al., 2020)).

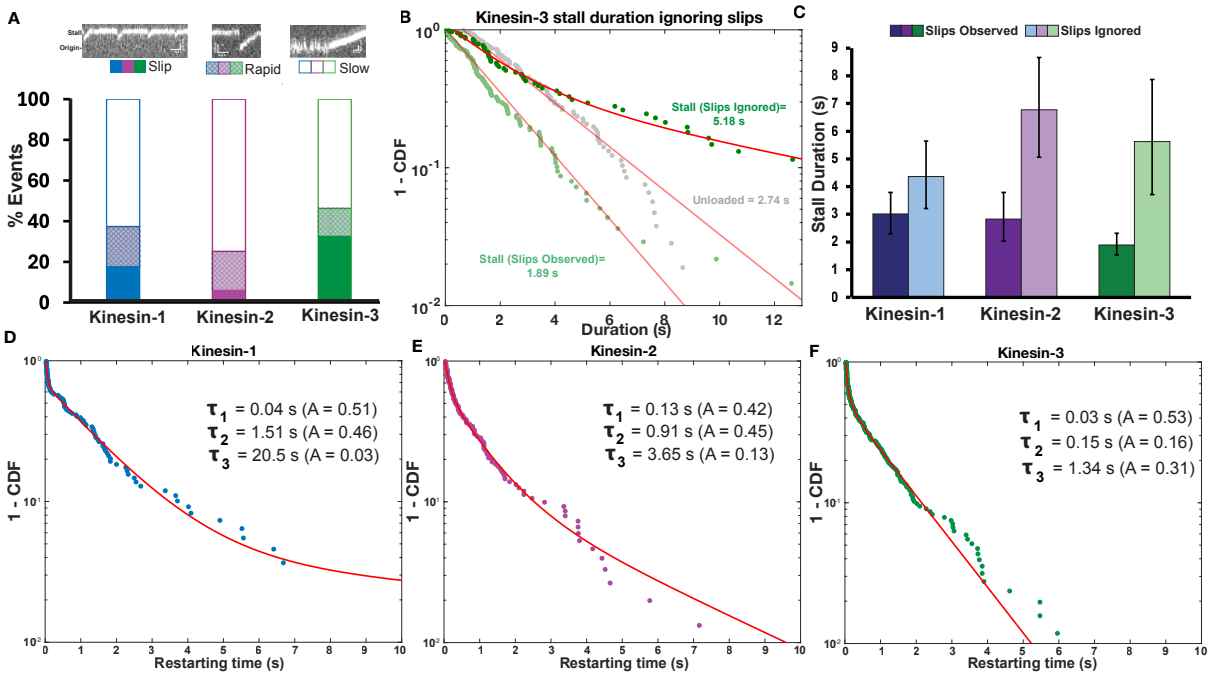

Figure 4. Restart Kinetics for Kinesin-1, -2 and -3. (A) Fraction of slip, fast rebinding, and slow rebinding events for each motor, with example kymographs for each (top). Solid colors indicate slips during stall, where the motor resumes a new ramp within a single frame (~40 ms), crosshatching indicates rapid reattachment events (100 ms) following fall to baseline, and open bars indicate slow reattachment events with >100 ms fluctuations around baseline.(B) Kinesin-3 stall durations, with unloaded run times in gray, stall durations terminated by slips in light green, and stall durations terminated by falling to the baseline (ignoring slips) in dark green. Unloaded and stall durations (replotted from Figure 2) were fit with single exponential functions in MEMLET. Stall durations ignoring slips were fit with a bi-exponential by least squares (τ_1 = 2.01 s [95% CI: 1.52, 2.35 s], A_1 = 0.66 s [0.54, 0.83 s], τ_2 = 11.0 s [9.18, 13.70], A_2 = 0.33 [0.23, 0.48]). Weighted average of the two time constants is displayed in plot for comparison to other time constants. Similar results for kinesin-1 and -2 are shown in Figure S7. (C) Comparison of stall durations for kinesins -1, -2 and -3 with slips observed as stall terminations or ignored. (D-F) Distribution of restart times for each motor fit to a tri-exponential (least squares). Confidence intervals of parameters determined by bootstrapping with 1000 iterations are given in Table S3.

Simulating Potential Catch-Bond Mechanisms

To compare the motor detachment and reattachment kinetics between the three kinesin transport families, we carried out stochastic simulations of load-dependent motor stepping, unbinding and rebinding. For simplicity, we reduced the chemomechanical cycle down to a single strongly-bound state (ATP and nucleotide-free states) and a single weakly-bound state (ADP and ADP-Pi states) (Figure 5A). Based on the published load and ATP dependencies of substeps in the kinesin-1 chemomechanical cycle (Sudhakar et al., 2021), we incorporated a load-dependent strong-to-weak transition, $k_{s\text{-}w}$ and a load-independent weak-to-strong transition, $k_{w\text{-}s}$. Based on our restarting durations from Figure 4 and previous work (Jannasch et al., 2013; Siddiqui et al., 2022; Sudhakar et al., 2021; Toleikis et al., 2020), we included both a slip state, from which the motor recovers rapidly, and a detached state associated with a slower recovery. Runs or stalls are terminated by transition from the weakly-bound state into the slip state (k_{slip}). Based on backstepping rates observed in

optical tweezer experiments, we incorporated a load-independent backward stepping rate of 3 s^{-1}, meaning that stall is defined as the load at which forward stepping slows to 3 s^{-1} (Carter & Cross, 2005; Coppin et al., 1997). For simplicity, we set $k_{s\text{-}w} = k_{w\text{-}s}$ at zero load, meaning that the motor spends half of its cycle in each state, (Mickolajczyk et al., 2015) with the rates set to match the unloaded velocity for each motor.

Using parameters chosen to match motor behavior under no load (Figure 5B), we were able to reproduce the unloaded run durations for all three motors (Figure 5C-E). Additionally, by using a slower $k_{S\text{-}W}$ and a faster k_{slip}, we could fit the kinesin-3 ramp data (Figure 5E), which we interpret to be more representative of the actual entry into the slip state (rather than remaining electrostatically associated with the microtubule under zero load). We next examined the behavior under load. The load-dependence of the strong-to-weak transition was set to match a 3 s^{-1} forward stepping rate at stall (balanced by a 3 s^{-1} backstepping rate). This was achieved by an exponential dependence on force, $k(F) = k_0 e^{\frac{F\delta}{k_B T}}$, with $k_{S\text{-}W}$ distance parameter, δ of -2.7, -2.4, and -3.6 nm for kinesin-1, -2 and -3, respectively. Importantly, this means that under increasing loads the motor spends a larger fraction of its cycle in the strongly-bound state. However, this formulation of the model predicted stall durations of tens of seconds (24 s, 20 s, and 176 s for kinesin-1, -2 and -3, respectively; Figure S8A), considerably longer than experimentally measured values. To remedy this, we incorporated a load dependence into to the transition to the slip state, such that slips occur more readily under load (k_{slip} δ of 1.6, 1.3 and 2.7 nm, respectively). With these parameters (Figure 5B), we were able to reproduce the stall duration distribution for all three motors (Figure 5C-E). Importantly, this model generates catch-bond behavior without requiring a protein-protein interaction having a dissociation rate that decreases with load (Thomas et al., 2008). Instead, detachment from the weakly-bound state is a slip bond (the dissociation rate increases with load), but by shifting the fraction of the cycle the motor spends in this vulnerable state, a catch-bond behavior is achieved.

To complete our model, we simulated recovery from the slip and detached states. The rate of rescue from the slip state (k_{resc}) was set based on the duration and relative amplitude of the fast phase of the restarting times in Figure 4. We posited that detachment follows the slip state, consistent with previous formulations (Sudhakar et al., 2021; Toleikis et al., 2020). The two slower restarting time constants from Figure 4 were used to set the reattachment rates, k_{reatt} (see Supplementary Methods for details). Using this approach, we were able to reproduce the restarting durations for all three motors (Figure 5F-H).

The rate constants derived from this model allow for a comparison of the specific transitions that differ between the three motor families. Three features are notable. First, for kinesin-3 the transition into the slip state at stall, k_{slip}, is the fastest of the three families, consistent with the observation by eye of the plateaus (Figure 1H and 4A) and consistent with previous three-bead optical trapping results (Pyrpassopoulos et al., 2023). Second, the rates of rescue from the slip state, k_{resc}, for the three motors match within a factor of two. Thus, the fast bimolecular on-rates from stopped flow and the relatively short durations before restarting we observe for kinesin-3 (Figure 4) do not result from a faster reengagement out of the slip state. Third, the slow reattachment rate for kinesin-3 is 10-fold faster than for kinesin-1 and -2. Hence, in this model formulation

the fast bimolecular on-rates and short restart durations observed for kinesin-3 result from recovery from a detached state rather than rescue from a slip state.

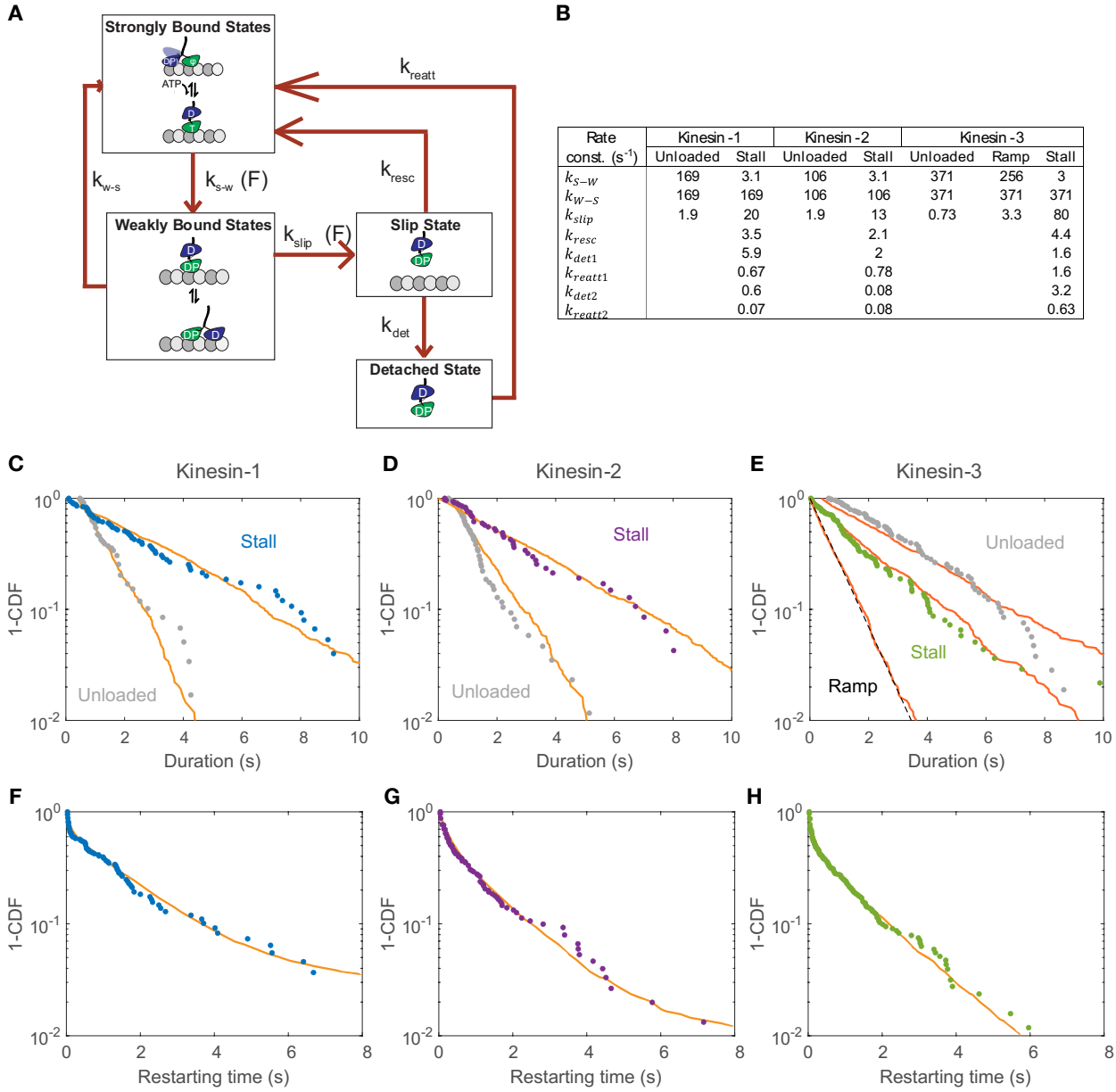

Rate const. (s^{-1})	Kinesin -1		Kinesin -2		Kinesin -3		
	Unloaded	Stall	Unloaded	Stall	Unloaded	Ramp	Stall
k_{S-W}	169	3.1	106	3.1	371	256	3
k_{W-S}	169	169	106	106	371	371	371
k_{slip}	1.9	20	1.9	13	0.73	3.3	80
k_{resc}		3.5		2.1			4.4
k_{det1}		5.9		2			1.6
k_{reatt1}		0.67		0.78			1.6
k_{det2}		0.6		0.08			3.2
k_{reatt2}		0.07		0.08			0.63

Figure 5. Chemomechanical Model of Proposed Catch-bond Mechanism. (A) Diagram of kinesin chemomechanical cycle model consisting of strongly- and weakly-bound states that make up the stepping cycle, and slip and detached states that terminate runs and stalls. (B) Table of rate constants used to simulate unloaded and stall durations and restarting times. All rate constants are derived from fits to experimental data, as described in Supplemental Methods. (C-E) Experimental (symbols) and simulated (lines) unloaded and stall durations. 10000 events were simulated for each condition and plotted with minimum cutoffs matching experiments. Kinesin-3 ramp durations are taken from parameter estimated in Figure 3. (F-H) Experimental (symbols) and simulated (lines) restart times.

Discussion

Understanding how motors respond vectorially to external loads is crucial for understanding cargo transport in complex intracellular geometries and how kinesin motors compete against dynein in bidirectional transport (Cason & Holzbaur, 2022; Hancock, 2014). Optical tweezer experiments have provided many essential details of the kinesin mechanochemical cycle under load; however, the bead diameters needed to achieve substantial trapping forces impose vertical forces on the motors, complicating the interpretation of load-dependent off-rate measurements and constraining how motors reengage following detachment. Using DNA as a nanospring enables motor protein mechanical experiments using a standard TIRF microscope, which allows for simultaneous monitoring of numerous motor-DNA complexes in a single imaging field. In previous work similar approaches have been used to study myosin, dynein and kinesin-1 in both single-molecule and gliding assays (Diez et al., 2003; Iwaki et al., 2016; Kuo et al., 2022; Nick Maleki et al., 2023; Shukla et al., 2022; Urbanska et al., 2021). With this geometry, a kinesin motor pulls against the elastic force of a stretched DNA solely in a direction parallel to the microtubule, matching the geometry of vesicles measuring a few tens of nanometers. Following disengagement, the motor is able to reengage with the microtubule without constraints from bead rotation. The most striking observation was that members of all three kinesin transport families show catch-bond behavior in which off-rates at stall are slower than those at low or zero loads. Additionally, following disengagement from the microtubule, the three motor families reengaged with the microtubule with complex and variable kinetics.

Comparison to previous work

Despite the clear slip-bond behavior of kinesin-1 seen in single-bead optical traps, there has been growing evidence that kinesin-1 detachment is sensitive to the direction of load. Motor engagement times were shown to decrease when larger beads were employed in single-bead traps, and to be extended in three-bead geometries that minimize vertical forces (Pyrpassopoulos et al., 2020). In a study that employed DNA-tethered kinesin-1 to extract tubulin the microtubule lattice, pulling durations of ~30 s were observed at the lowest motor concentrations, indicative of catch-bond behavior (Kuo et al., 2022). When kinesin-1 was tethered to a glass coverslip via a DNA linker and hydrodynamic forces were imposed on an associated microtubule, kinesin-1 dissociation rates were relatively insensitive to loads up to ~3 pN, inconsistent with slip-bond characteristics (Urbanska et al., 2021). The 3 s kinesin-1 stall duration in our tensiometer falls between 30 s value for tubulin pulling and the 1.3 s median engagement time measured in the three-bead trap. In contrast, kinesin-3 (KIF1A) median engagement durations were found to be similarly short in the one-bead (69 ms) and three bead (62 ms) geometries (Pyrpassopoulos et al., 2023), much shorter than our 1.9 s stall duration in the DNA tensiometer. One difference may be that very fast (~millisecond) slips observed in the optical tweezer measurements were counted as termination events, and thus limited engagement times. However, despite the slower (~25 frames/s) temporal resolution of our measurements, we expect that short duration slipping events should produce a rapid recoil of the DNA that generates easily detected displacements. One difference is that in the three-bead experiment, the microtubule is

held under tension, which may alter the lattice properties. Furthermore, it can't be ruled out that KIF1A is particularly sensitive to vertical loads and small lateral or vertical forces present in the three-bead geometry are absent in the DNA tensiometer geometry. To date there have been no studies on kinesin-2 where vertical loads are minimized, and in single-bead optical traps the off-rate depends strongly on load .

Transport kinesins have a catch-bond behavior under hindering loads

What is the mechanism of the observed catch-bond behavior? Cell adhesion proteins such as integrins, selectins, and FimH have been shown to form longer lasting bonds under load, with the proposed mechanisms generally involving an allosteric effect that strengthens the protein:protein interface (Kong et al., 2009; Marshall et al., 2003; Thomas et al., 2002). However, motor proteins are different in that they cycle in a nucleotide-dependent way between strongly- and weakly bound states, offering multiple potential mechanisms for slower dissociation rates under load. For instance, under a few piconewtons of load, Myosin I was shown to dissociate nearly two orders of magnitude slower than in the absence of load, an effect attributed to load-dependent trapping of ADP in the active site that maintained the motor a high-affinity binding state (Laakso et al., 2008). Dynein was also shown to have catch-bond behavior over certain ranges of resisting loads, though the precise mechanism is unclear (Kunwar et al., 2011; Rai et al., 2016; Rai et al., 2013; Sanghavi et al., 2021).

We interpreted our stepping, detachment, and reattachment results using a model that incorporates a load-dependent strong-to-weak transition and a load-dependent entry into a transient 'slip' state preceding detachment. The key feature of the model is that under load the motor spends an increasing fraction of its hydrolysis cycle in a strongly-bound state that resists dissociation.

The role of vertical forces in motor detachment

We next asked whether by considering the different geometries we could reconcile our catch-bond observations with previous single-bead optical tweezer kinesin-1 slip-bond measurements that found the kinesin-1 off-rate increased from 1.11 s^{-1} at zero load to 2.67 s^{-1} at 6 pN (Andreasson et al., 2015). Using a 440 nm bead diameter and estimated motor length of 35 nm that results in the force being imposed on the motor at a 60º angle (Figure S8B), a 6 pN stall force parallel to the microtubule corresponds to a 10 pN force perpendicular to the microtubule (Andreasson et al., 2015; Khataee & Howard, 2019). A model developed by Khataee and Howard was able to fully account for these geometry-dependent off-rates using a two-step detachment process having catch-bond behavior for parallel loads and slip-bond behavior for vertical loads (Khataee & Howard, 2019). Applying that model to our geometry and assuming a purely horizontal load and a 6 pN stall force, the predicted stall duration for kinesin-1 is 77 s, much longer than the 3 s we measure (Figure S8). We approached the detachment process differently, by incorporating a load-dependent transition in the hydrolysis cycle ($k_{S\text{-}W}$) and a load-dependent exit from the hydrolysis cycle (k_{slip}). To explore effects of vertical forces using our two-state model, we incorporated both horizontal and vertical loads as accelerating detachment from the weakly-bound state, as follows:

$$k_{slip}(F) = k_{slip}^{0} e^{\frac{(F_{\parallel}\delta_{\parallel} + F_{\perp}\delta_{\perp})}{k_B T}}$$

Here $F_{\parallel}$ and $F_{\perp}$ are the magnitude of the parallel and perpendicular loads and $\delta_{\parallel}$ and $\delta_{\perp}$ represent the distance parameters in each direction (Figure S8). Using $\delta_{\parallel}$ = 1.61 nm (Figure 5B), we found that by setting $\delta_{\perp}$ = 1.58 nm, we were able to reproduce the slip bond behavior observed in the single-bead optical trap experiments (Figure S8). Notably, this model implies that vertical and horizontal forces have similar effects on the transition rate into the slip state. We stress that this model is a hypothesis that needs further testing. Nonetheless, this is a simple formulation that shows that a motor can display either catch bond or slip bond behavior depending on the geometry of the imposed loads.

Ramps reveal detachment behaviors at low loads

In addition to reporting on the detachment properties at stall, our DNA tensiometer provides new insights into fast rebinding that occurs during unloaded runs of kinesin-3. It has long been appreciated that the kinesin-3 motor KIF1A achieves long run lengths due to electrostatic attraction between its positively charged Loop-12 (K-loop) and the negatively charged C-terminal tail of tubulin (Lessard et al., 2019; Okada et al., 2003; Okada & Hirokawa, 1999, 2000; Soppina et al., 2014; Soppina & Verhey, 2014; Zaniewski et al., 2020; Zaniewski & Hancock, 2023). Furthermore, the KIF1A off-rate in ADP, in which the motor diffuses on the microtubule lattice, was found to match the off-rate during processive stepping in ATP (Zaniewski et al., 2020). The relatively high microtubule affinity of this weakly-bound state suggests that the motor may be undergoing diffusive episodes between processive runs, while maintaining association with the microtubule.

Our DNA tensiometer offers a way to test the hypothesis that the long, unloaded run lengths of KIF1A are due to a concatenation of shorter runs. Due to the nonlinearity of the dsDNA force-extension curve in our DNA tensiometer, the motor is walking against forces below 1 pN for roughly 90% of the distance to stall (Figure 1B). Consistent with this, motor velocities were nearly constant until they were near the stall force (Figure 1D and S3), and ramp velocities averaged only ~15% slower than unloaded velocities (Table S1), which corresponds to ~1 pN of force if the force-velocity relationship is linear. Using a Bayesian Inference approach that takes into account motors that dissociate during the ramps as well as those that complete ramps by achieving stall, we measured a nearly four-fold faster KIF1A detachment rate during ramps than under zero load (Figure 3). If, under zero load, the long runs observed were actually a concatenation of a series of shorter runs connected by diffusive weakly-bound events, the diffusive state would likely be unable to withstand even the sub-pN forces from the DNA spring (Okada & Hirokawa, 2000). For instance, based on a 0.044 $\mu m^2/s$ diffusion coefficient (equivalent to a ~0.1 pN-s/μm drag coefficient (Howard, 2001; Okada & Hirokawa, 2000)), if the motor were in a weakly-bound state for 10 ms, a 1 pN force would pull the motor back 100 nm. Thus, in considering whether KIF1A acts as a catch bond, we used this ramp duration as the best approximation for the true run unloaded length in the absence of diffusive events.

The ramp durations of kinesin-1 and kinesin-2 also provide insights into how load alters their interactions with microtubules. For kinesin-2, the predicted ramp duration

was not statistically different from the unloaded run duration, suggesting that unloaded runs do not include short diffusive episodes. This result is somewhat surprising, given previous kinesin-2 force-clamp optical tweezer experiments that found a substantial drop in run length between the unloaded case and the lowest force (1 pN) and a smooth reduction in run length at higher forces (; Figure 4A). However, this discrepancy may be due to vertical forces associated with the single bead geometry accelerating the detachment rate in the optical tweezer study (Khataee & Howard, 2019). Interestingly the predicted ramp duration for kinesin-1 was nearly the same as the stall duration and much longer than the unloaded duration. One possibility is that the catch-bond effect of hindering load comes into play at low loads and not only at stall where the motor has slowed considerably.

Motor slips and detachments reflect different processes

Because the DNA tensiometer tethers the motor near the microtubule, such that repeated binding and unbinding events occur, it enables comparison of family-dependent differences in kinesin rebinding kinetics. In addition to clear detachment events, rapid slip and recovery events were observed for all three motors, with highest frequency for kinesin-3 and lowest frequency for kinesin-1. Backwards slipping while maintaining association with the microtubule was first seen for kinesin-8 motors, which are highly processive yet generate only small forces(Jannasch et al., 2013). Under both hindering and assisting loads, displacements of multiples of 8 nm were observed, consistent with the motor remaining associated with the microtubule and rebinding to a neighboring tubulin. Similar slips were observed for kinesin-1, and the plateaus that preceded the slips were longer duration than the plateaus preceding forward steps, suggesting that the motor transitioned into a different state preceding the slip, such as phosphate dissociation to generate the ADP state. Subsequent higher resolution work, enabled by small Germanium nanoparticles, revealed a staircase pattern during these slips with ~8 nm steps of mean duration 73 μsec, suggesting that the motor was transiently interacting with each tubulin subunit as it slipped backward. Similar slips have also been observed for kinesin-2 , and two kinesin-3 family members, KIF1A and KIF1C (Pyrpassopoulos et al., 2023; Siddiqui et al., 2022).

There is some dispute in the literature regarding the kinetics of the recovery from the slip state for kinesin-1. Using a single-bead trap, Sudhakar found that 80% of restart events were slips with a time constant of 128 ms (Sudhakar et al., 2021), whereas Toleikis measured slip recoveries that were essentially at the limit of detection (~msec) (Toleikis et al., 2020). Using a three-bead trap, Pyrpassopoulis measured a 10 ms slip time constant for kinesin-1 (Pyrpassopoulos et al., 2020). Our 40 ms slip time constant, which accounts for half of recovery events, is limited by the camera frame rate, and thus is likely an overestimate. In the three-bead geometry kinesin-3 (KIF1A) slips recovered with a time constant of 1 ms (Pyrpassopoulos et al., 2023), faster than the 30 msec (upper limit estimate) we observe. Thus, the precise recovery rate is dependent on the detailed measurement and analysis used. In our DNA tensiometer results, the higher frequency of slips for kinesin-3 relative to kinesin-1 is seen by direct counting (Figure 4A), by the large enhanced stall duration when slips are not counted as termination events (Figure 4C), and by the fast k_{slip} parameter under load in the kinesin-3 model (Figure 5B).

Catch-bond behavior provides insights into tug-of-war with dynein

Consistent with the diversity of intracellular cargo transported by kinesin and dynein, there are many features such as motor number and type, microtubule isotype, and cargo size and geometry that can regulate transport. In previous simulations of kinesin-dynein tug-of-war transport, we found that the strongest determinants of kinesin's ability to compete against dynein were the load-dependent motor dissociation rate and the motor rebinding rate (Ma et al., 2023; Ohashi et al., 2019). Simply put, if motors detach, then the opposing motor wins, and if they remain attached against strong antagonistic loads, they can at least achieve a stalemate against their opposition. The finding here that all three dominant kinesin transport families display catch-bond behavior at stall necessitates a reevaluation of how motors function during a tug-of-war. There is evidence that dynein forms a catch bond or at least an ideal (load independent) bond (Belyy et al., 2016; Cianfrocco et al., 2015; Kunwar et al., 2011; Rai et al., 2016; Rai et al., 2013; Sanghavi et al., 2021); thus, kinesins and dyneins are primed to strongly oppose one another. Consistent with this, when vesicle motility is quantified during axonal transport, there are often a large fraction of immobile vesicles and even those that move include sustained immobile episodes (Encalada et al., 2011; Fu & Holzbaur, 2013; Gross et al., 2002; Hancock, 2014; Iacobucci et al., 2014). It's possible that no motors are engaged in these cases, but it's also possible that the motors are stalled in a tug-of-war with the large antagonistic forces suppressing the kinesin and dynein off-rates.

The catch bond results here help to explain previous in vitro work in which one kinesin and one dynein were connected through a complementary ssDNA (Belyy et al., 2016; Feng et al., 2020; Gicking et al., 2022). It was found that the motor pairs had periods of near-zero velocity that lasted for many seconds, considerably longer than kinesin's unloaded off-rate. Furthermore, kinesin-2 and kinesin-3 also showed these sustained slow tug-of-war periods despite their reported faster load-dependent off-rates from optical tweezer studies. The functional catch-bond behavior observed here provides a simple explanation for these sustained kinesin-dynein stalemates.

Importantly, the load-dependent off-rates of both kinesins and dynein are expected to depend on the cargo geometry. A 30 nm vesicle would lead to forces on the motor nearly parallel to the microtubule surface, whereas when transporting a micron-scale mitochondria the vertical forces would be larger than the horizontal forces. Cargo geometry and stiffness is also expected to play a role; for instance, deformation of a cargo, either due to compliance of the cargo or to multiple motors pulling on it will tend to reduce vertical force components on the motors. The present work emphasizes that along with motor type, motor number, motor autoinhibition, and the growing list of regulatory proteins, the geometry with kinesin and dynein engage in a tug-of-war can be an important determinant of the speed and direction of cargo transport in cells.

Methods

DNA Tensiometer Construction

For the dsDNA spring, a 5' biotinylated forward primer (5'-/5Biosg/TGC CTC CGT GTA AGG GGG AT-3') and a reverse primer with a 5' overhang (5'-/GGG CCA TCG

CCA ATT GGA GTA /idSp/ GTG AGT TAA AGT TGT ACT CGA GTT TGT GTC CAA GAA -3') were used to create a 3009 bp dsDNA by PCR from plasmid *Mus Musculus* BicD2-sf-GFP (aa 25-425) in pet28a. The abasic Int 1',2'-Dideoxyribose spacer (idSp) creates an overhang by terminating the polymerase. All oligonucleotides were purchased from IDT. Each 50 μL PCR reaction contained: 1x Phusion HF buffer, 198 μM dNTPs, 2 μM dCTP-Cy5, 0.5 μM primers, 3 ng template DNA and 1 U/50 μL HF Phusion Polymerase. Fluorescent dsDNA used in Figure S4 had 10μM dCTP-Cy5 and 190μM dNTPs. The PCR reaction was carried out in a thermal cycler with the following procedure: 98℃ for 30 s, then 45 cycles of 98℃ for 10 s, 58℃ for 30 s and 72℃ for 1.5 min, then lastly 72℃ for 5 min. The product was purified using a NucleoSpin® PCR clean-up kit and the concentration determined by absorbance on a Nanodrop 2000c Spectrophotometer. DNA bands were visualized on a 1% agarose gel with ethidium bromide staining.

Motor-Microtubule-Tensiometer Assembly

Motors were bacterially expressed, purified and linked through its SNAP tag to an oligonucleotide (5'-/TAC TCC AAT TGG CGA TGG CCC / 3AmMC6T/-3') complementary to the dsDNA overhang. Details of motor expression, purification and labeling, as well as tubulin biotinylation and polymerization are given in Supplementary Information. The DNA tensiometer was assembled on the microtubule as follows. The following three buffers are made on the same day of the experiment: C2AT (BRB80, 10 μM Taxol, 2 mM MgATP, 2 mg/mL Casein), 2AT (BRB80, 10 μM Taxol, 2 mM MgATP) and Imaging Solution (BRB80, 10 μM Taxol, 2 mg/mL Casein, 2 mM MgATP, 20 mM D-glucose, 0.02 mg/mL Glucose oxidase, 0.008 mg/mL Catalase, 0.5% BME and 2 mg/mL BSA). Full-length rigor kinesin was used to attach microtubules to the coverglass (Mickolajczyk et al., 2015). Tensiometers were created in the flow cell using the following work flow: C2AT, 5 min > Rigor kinesin, 5 min> C2AT wash > BioMT, 5 min > 2AT > 8 nM Neutravidin, 5 min> 2AT > 10 nM Bio-dsDNA-Overhang, 5 min> C2AT > 4 nM KinesinMotor + 40nM Qdot-GBP (pre incubated in tube on ice for >15 min) in imaging solution, 10 min > Imaging solution wash. Note that because casein can contain free biotin, casein-free 2AT buffer was used during avidin-biotin binding steps. Following assembly, the Qdot connected to the motor was imaged on a custom-built TIRF microscope, described previously (Nong et al., 2021). Raw data were typically collected at 25 fps (range of 20-40 fps) on a Photometrics Prime 95B camera.

Data Analysis

Movies were uploaded into FIESTA software (Ruhnow et al., 2011) and Qdot intensities were tracked using a symmetric 2-D gaussian function to obtain x,y,t data for each Qdot. When drift correction was needed, TetraSpeck™ Fluorescent Microspheres (Thermo) and immobile Qdots were used as fiducial markers. The smallest position errors at stall in FIESTA fitting were 3-4 nm, which matched the positional error of Qdot-labeled motors stuck to microtubules in AMPPNP. Points with position errors greater than 20 nm were excluded because they often involved clearly spurrious position estimates. Notably, many tensiometers had small segments of missing data due to the Qdot fluctuating out of the TIRF field or blinking; these occurred most often during periods when the motors were detached from the microtubule.

After obtaining X and Y positions of linear motor tracks in Fiesta, we rotated and translated the data in Excel to generate X versus t traces. The apparent origin was determined by averaging the points where the motor is fluctuating on its tether. In rare instances where no fluctuation was observed, the approximate origin was calculated by averaging the starting positions of all the ramps within the tensiometer (Figure 1). We then measured the ramp time, distance traveled, stall durations, reattachment times and starting positions. Tensiometers occasionally ended with the Qdot signal going dark, denoting either bleaching or failure of the Qdot-motor or motor-DNA connection. Notably, no clear instances of motor-Qdots walking past the plateau point (denoting the tensiometer breaking) were observed. Stalls that terminated due to the tensiometer going dark or the video ending were excluded from analysis.

Stochastic Modeling

Kinesin run and stall durations were simulated by using a modified version of published stochastic model of kinesin stepping (Gicking et al., 2022; Ma et al., 2023). A motor is either in a strongly-bound state or a weakly-bound state (Figure 5A). At each timepoint, a motor in the strongly bound state can transition into the weakly-bound state with a first order transition rate constant, k_{S-W} or step backward by 8 nm with a constant rate, $k_{back} = 3\ s^{-1}$. A motor in the weakly-bound state can complete an 8-nm forward step by transitioning back to the strongly-bound state with rate constant, k_{W-S}, or it can disengage from the microtubule with transition rate, k_{slip}.

For simplicity, we set $k_{S-W} = k_{W-S}$ at zero load. Load-dependent transition rates were defined as:

$$k(F) = k^0 * e^{\frac{F\delta}{k_B T}}$$

where k^0 is the unloaded transition rate, δ is the characteristic distance parameter and $k_B T$ is the Boltzmann's constant multiplied by the absolute temperature, equal to 4.1 pN-nm at $25°$ C. Stall force was set to 6 pN. Unloaded and stall durations were simulated by starting the motor in strongly-bound state and continuing until it transitioned into the slip state, with 1000 simulations for each condition. Restart times were simulated by starting the motor in the slip state. From there, the motor can reengage by transitioning into the strongly-bound state or switch to one of two detached states having either a slow or fast recovery rate. Restart simulations were run for 10,000 iterations. Model parameters were constrained by experimental data, described fully in Supplementary Methods.

Acknowledgments

This work was originally conceived as part of a NIH-funded collaborative modeling project to Will Hancock, Scott McKinley, John Fricks, and Peter Kramer (R01GM122082). We thank Qingzhou Feng, Scott Pflumm, and Adheshwari Ramesh for early efforts on this project and all members of the Hancock Lab for helpful discussions. This work was funded by NIH Grant R35GM139568 to W.O.H.. C.R.N. was supported by NIH postdoctoral fellowship F32GM149114, R.J. was supported by NIH Training Grant T32GM108563, and S.A.M. was supported by the NSF-Simons Southeast Center

for Mathematics and Biology (SCMB) through grant NSF-DMS1764406 and Simons Foundation-SFARI 594594.

References

Andreasson, J. O., Milic, B., Chen, G. Y., Guydosh, N. R., Hancock, W. O., & Block, S. M. (2015). Examining kinesin processivity within a general gating framework. *Elife*, *4*. https://doi.org/10.7554/eLife.07403

Bell, G. I. (1978). Models for the specific adhesion of cells to cells. *Science*, *200*(4342), 618-627. https://doi.org/10.1126/science.347575

Belyy, V., Schlager, M. A., Foster, H., Reimer, A. E., Carter, A. P., & Yildiz, A. (2016). The mammalian dynein-dynactin complex is a strong opponent to kinesin in a tug-of-war competition. *Nat Cell Biol*, *18*(9), 1018-1024. https://doi.org/10.1038/ncb3393

Blehm, B. H., Schroer, T. A., Trybus, K. M., Chemla, Y. R., & Selvin, P. R. (2013). In vivo optical trapping indicates kinesin's stall force is reduced by dynein during intracellular transport. *Proc Natl Acad Sci U S A*, *110*(9), 3381-3386. https://doi.org/10.1073/pnas.1219961110

Brenner, D., Yilmaz, R., Muller, K., Grehl, T., Petri, S., Meyer, T., Grosskreutz, J., Weydt, P., Ruf, W., Neuwirth, C., Weber, M., Pinto, S., Claeys, K. G., Schrank, B., Jordan, B., Knehr, A., Gunther, K., Hubers, A., Zeller, D.,…German, A. L. S. n. M. N. D. N. E. T. (2018). Hot-spot KIF5A mutations cause familial ALS. *Brain*, *141*(3), 688-697. https://doi.org/10.1093/brain/awx370

Budaitis, B. G., Jariwala, S., Rao, L., Yue, Y., Sept, D., Verhey, K. J., & Gennerich, A. (2021). Pathogenic mutations in the kinesin-3 motor KIF1A diminish force generation and movement through allosteric mechanisms. *J Cell Biol*, *220*(4). https://doi.org/10.1083/jcb.202004227

Caballero Oteyza, A., Battaloglu, E., Ocek, L., Lindig, T., Reichbauer, J., Rebelo, A. P., Gonzalez, M. A., Zorlu, Y., Ozes, B., Timmann, D., Bender, B., Woehlke, G., Zuchner, S., Schols, L., & Schule, R. (2014). Motor protein mutations cause a new form of hereditary spastic paraplegia. *Neurology*, *82*(22), 2007-2016. https://doi.org/10.1212/WNL.0000000000000479

Carter, N. J., & Cross, R. A. (2005). Mechanics of the kinesin step. *Nature*, *435*(7040), 308-312. https://doi.org/10.1038/nature03528

Cason, S. E., & Holzbaur, E. L. F. (2022). Selective motor activation in organelle transport along axons. *Nat Rev Mol Cell Biol*, *23*(11), 699-714. https://doi.org/10.1038/s41580-022-00491-w

Chen, G. Y., Arginteanu, D. F., & Hancock, W. O. (2015). Processivity of the kinesin-2 KIF3A results from rear head gating and not front head gating. *J Biol Chem*, *290*(16), 10274-10294. https://doi.org/10.1074/jbc.M114.628032

Cianfrocco, M. A., DeSantis, M. E., Leschziner, A. E., & Reck-Peterson, S. L. (2015). Mechanism and regulation of cytoplasmic dynein. *Annu Rev Cell Dev Biol*, *31*, 83-108. https://doi.org/10.1146/annurev-cellbio-100814-125438

Coppin, C. M., Pierce, D. W., Hsu, L., & Vale, R. D. (1997). The load dependence of kinesin's mechanical cycle. *Proc Natl Acad Sci U S A*, *94*(16), 8539-8544. https://doi.org/10.1073/pnas.94.16.8539

D'Souza, A. I., Grover, R., Monzon, G. A., Santen, L., & Diez, S. (2024). Publisher Correction: Vesicles driven by dynein and kinesin exhibit directional reversals without regulators. *Nat Commun*, *15*(1), 736. https://doi.org/10.1038/s41467-024-45256-5

Diez, S., Reuther, C., Dinu, C., Seidel, R., Mertig, M., Pompe, W., & Howard, J. (2003). Stretching and Transporting DNA Molecules Using Motor Proteins. *Nano Lett*, *3*(9), 1251-1254.

Encalada, S. E., Szpankowski, L., Xia, C. H., & Goldstein, L. S. (2011). Stable kinesin and dynein assemblies drive the axonal transport of mammalian prion protein vesicles. *Cell*, *144*(4), 551-565. https://doi.org/10.1016/j.cell.2011.01.021

Ezber, Y., Belyy, V., Can, S., & Yildiz, A. (2020). Dynein Harnesses Active Fluctuations of Microtubules for Faster Movement. *Nat Phys*, *16*, 312-316. https://doi.org/10.1038/s41567-019-0757-4

Feng, Q., Gicking, A. M., & Hancock, W. O. (2020). Dynactin p150 promotes processive motility of DDB complexes by minimizing diffusional behavior of dynein. *Mol Biol Cell*, *31*(8), 782-792. https://doi.org/10.1091/mbc.E19-09-0495

Feng, Q., Mickolajczyk, K. J., Chen, G. Y., & Hancock, W. O. (2018). Motor Reattachment Kinetics Play a Dominant Role in Multimotor-Driven Cargo Transport. *Biophys J*, *114*(2), 400-409. https://doi.org/10.1016/j.bpj.2017.11.016

Fu, M. M., & Holzbaur, E. L. (2013). JIP1 regulates the directionality of APP axonal transport by coordinating kinesin and dynein motors. *J Cell Biol*, *202*(3), 495-508. https://doi.org/10.1083/jcb.201302078

Gicking, A. M., Ma, T. C., Feng, Q., Jiang, R., Badieyan, S., Cianfrocco, M. A., & Hancock, W. O. (2022). Kinesin-1, -2, and -3 motors use family-specific mechanochemical strategies to effectively compete with dynein during bidirectional transport. *Elife*, *11*. https://doi.org/10.7554/eLife.82228

Gross, S. P. (2004). Hither and yon: a review of bi-directional microtubule-based transport. *Phys Biol*, *1*(1-2), R1-11. https://doi.org/10.1088/1478-3967/1/2/R01

Gross, S. P., Welte, M. A., Block, S. M., & Wieschaus, E. F. (2002). Coordination of opposite-polarity microtubule motors. *J Cell Biol*, *156*(4), 715-724. https://doi.org/10.1083/jcb.200109047

Hancock, W. O. (2014). Bidirectional cargo transport: moving beyond tug of war. *Nat Rev Mol Cell Biol*, *15*(9), 615-628. https://doi.org/10.1038/nrm3853

Hendricks, A. G., Perlson, E., Ross, J. L., Schroeder, H. W., 3rd, Tokito, M., & Holzbaur, E. L. (2010). Motor coordination via a tug-of-war mechanism drives bidirectional vesicle transport. *Curr Biol*, *20*(8), 697-702. https://doi.org/10.1016/j.cub.2010.02.058

Howard, J. (2001). *Mechanics of Motor Proteins and the Cytoskeleton*. Sinauer Associates.

Iacobucci, G. J., Rahman, N. A., Valtuena, A. A., Nayak, T. K., & Gunawardena, S. (2014). Spatial and temporal characteristics of normal and perturbed vesicle transport. *PLoS One*, *9*(5), e97237. https://doi.org/10.1371/journal.pone.0097237

Iwaki, M., Wickham, S. F., Ikezaki, K., Yanagida, T., & Shih, W. M. (2016). A programmable DNA origami nanospring that reveals force-induced adjacent binding of myosin VI heads. *Nat Commun*, *7*, 13715. https://doi.org/10.1038/ncomms13715

Jannasch, A., Bormuth, V., Storch, M., Howard, J., & Schaffer, E. (2013). Kinesin-8 is a low-force motor protein with a weakly bound slip state. *Biophys J*, *104*(11), 2456-2464. https://doi.org/10.1016/j.bpj.2013.02.040

Khataee, H., & Howard, J. (2019). Force Generated by Two Kinesin Motors Depends on the Load Direction and Intermolecular Coupling. *Phys Rev Lett*, *122*(18), 188101. https://doi.org/10.1103/PhysRevLett.122.188101

Kojima, H., Muto, E., Higuchi, H., & Yanagida, T. (1997). Mechanics of single kinesin molecules measured by optical trapping nanometry. *Biophys J*, *73*(4), 2012-2022. https://doi.org/10.1016/S0006-3495(97)78231-6

Kong, F., Garcia, A. J., Mould, A. P., Humphries, M. J., & Zhu, C. (2009). Demonstration of catch bonds between an integrin and its ligand. *J Cell Biol*, *185*(7), 1275-1284. https://doi.org/10.1083/jcb.200810002

Kunwar, A., Tripathy, S. K., Xu, J., Mattson, M. K., Anand, P., Sigua, R., Vershinin, M., McKenney, R. J., Yu, C. C., Mogilner, A., & Gross, S. P. (2011). Mechanical stochastic tug-of-war models cannot explain bidirectional lipid-droplet transport. *Proc Natl Acad Sci U S A*, *108*(47), 18960-18965. https://doi.org/10.1073/pnas.1107841108

Kuo, Y. W., Mahamdeh, M., Tuna, Y., & Howard, J. (2022). The force required to remove tubulin from the microtubule lattice by pulling on its alpha-tubulin C-terminal tail. *Nat Commun*, *13*(1), 3651. https://doi.org/10.1038/s41467-022-31069-x

Laakso, J. M., Lewis, J. H., Shuman, H., & Ostap, E. M. (2008). Myosin I can act as a molecular force sensor. *Science*, *321*(5885), 133-136. https://doi.org/10.1126/science.1159419

Lessard, D. V., Zinder, O. J., Hotta, T., Verhey, K. J., Ohi, R., & Berger, C. L. (2019). Polyglutamylation of tubulin's C-terminal tail controls pausing and motility of kinesin-3 family member KIF1A. *J Biol Chem*, *294*(16), 6353-6363. https://doi.org/10.1074/jbc.RA118.005765

Ma, T. C., Gicking, A. M., Feng, Q., & Hancock, W. O. (2023). Simulations suggest robust microtubule attachment of kinesin and dynein in antagonistic pairs. *Biophys J*, *122*(16), 3299-3313. https://doi.org/10.1016/j.bpj.2023.07.007

Makrythanasis, P., Maroofian, R., Stray-Pedersen, A., Musaev, D., Zaki, M. S., Mahmoud, I. G., Selim, L., Elbadawy, A., Jhangiani, S. N., Coban Akdemir, Z. H., Gambin, T., Sorte, H. S., Heiberg, A., McEvoy-Venneri, J., James, K. N., Stanley, V., Belandres, D., Guipponi, M., Santoni, F. A.,…Antonarakis, S. E. (2018). Biallelic variants in KIF14 cause intellectual disability with microcephaly. *Eur J Hum Genet*, *26*(3), 330-339. https://doi.org/10.1038/s41431-017-0088-9

Marko, J. F., & Siggia, E. D. (1995). Stretching DNA. *Macromolecules*, *28*(26), 8759-8770. https://siggia.rockefeller.edu/Publications/1990-9_files/markoMacromol1995.pdf

Marshall, B. T., Long, M., Piper, J. W., Yago, T., McEver, R. P., & Zhu, C. (2003). Direct observation of catch bonds involving cell-adhesion molecules. *Nature*, *423*(6936), 190-193. https://doi.org/10.1038/nature01605

Mickolajczyk, K. J., Deffenbaugh, N. C., Arroyo, J. O., Andrecka, J., Kukura, P., & Hancock, W. O. (2015). Kinetics of nucleotide-dependent structural transitions in the kinesin-1 hydrolysis cycle. *Proc Natl Acad Sci U S A*, *112*(52), E7186-7193. https://doi.org/10.1073/pnas.1517638112

Millecamps, S., & Julien, J. P. (2013). Axonal transport deficits and neurodegenerative diseases. *Nat Rev Neurosci*, *14*(3), 161-176. https://doi.org/10.1038/nrn3380

Moawia, A., Shaheen, R., Rasool, S., Waseem, S. S., Ewida, N., Budde, B., Kawalia, A., Motameny, S., Khan, K., Fatima, A., Jameel, M., Ullah, F., Akram, T., Ali, Z., Abdullah, U., Irshad, S., Hohne, W., Noegel, A. A., Al-Owain, M.,…Hussain, M. S. (2017). Mutations of KIF14 cause primary microcephaly by impairing cytokinesis. *Ann Neurol*, *82*(4), 562-577. https://doi.org/10.1002/ana.25044

Muller, M. J., Klumpp, S., & Lipowsky, R. (2008). Tug-of-war as a cooperative mechanism for bidirectional cargo transport by molecular motors. *Proc Natl Acad Sci U S A*, *105*(12), 4609-4614. https://doi.org/10.1073/pnas.0706825105

Nick Maleki, A., Huis In 't Veld, P. J., Akhmanova, A., Dogterom, M., & Volkov, V. A. (2023). Estimation of microtubule-generated forces using a DNA origami nanospring. *J Cell Sci*, *136*(5). https://doi.org/10.1242/jcs.260154

Nong, D., Haviland, Z. K., Kuntz, K. V., Tien, M., Anderson, C. T., & Hancock, W. O. (2021). Integrated multi-wavelength microscope combining TIRFM and IRM modalities for imaging cellulases and other processive enzymes. *Biomed Opt Express*, *12*(6), 3253-3264. https://doi.org/10.1364/BOE.423798

Ohashi, K. G., Han, L., Mentley, B., Wang, J., Fricks, J., & Hancock, W. O. (2019). Load-dependent detachment kinetics plays a key role in bidirectional cargo transport by kinesin and dynein. *Traffic*, *20*(4), 284-294. https://doi.org/10.1111/tra.12639

Okada, Y., Higuchi, H., & Hirokawa, N. (2003). Processivity of the single-headed kinesin KIF1A through biased binding to tubulin. *Nature*, *424*(6948), 574-577. https://doi.org/10.1038/nature01804

Okada, Y., & Hirokawa, N. (1999). A processive single-headed motor: kinesin superfamily protein KIF1A. *Science*, *283*(5405), 1152-1157. https://doi.org/10.1126/science.283.5405.1152

Okada, Y., & Hirokawa, N. (2000). Mechanism of the single-headed processivity: diffusional anchoring between the K-loop of kinesin and the C terminus of tubulin. *Proc Natl Acad Sci U S A*, *97*(2), 640-645. https://doi.org/10.1073/pnas.97.2.640

Pant, D. C., Parameswaran, J., Rao, L., Loss, I., Chilukuri, G., Parlato, R., Shi, L., Glass, J. D., Bassell, G. J., Koch, P., Yilmaz, R., Weishaupt, J. H., Gennerich, A., & Jiang, J. (2022). ALS-linked KIF5A DeltaExon27 mutant causes neuronal toxicity through gain-of-function. *EMBO Rep*, *23*(8), e54234. https://doi.org/10.15252/embr.202154234

Pyrpassopoulos, S., Gicking, A. M., Zaniewski, T. M., Hancock, W. O., & Ostap, E. M. (2023). KIF1A is kinetically tuned to be a superengaging motor under hindering loads. *Proc Natl Acad Sci U S A*, *120*(2), e2216903120. https://doi.org/10.1073/pnas.2216903120

Pyrpassopoulos, S., Shuman, H., & Ostap, E. M. (2020). Modulation of Kinesin's Load-Bearing Capacity by Force Geometry and the Microtubule Track. *Biophys J*, *118*(1), 243-253. https://doi.org/10.1016/j.bpj.2019.10.045

Rai, A., Pathak, D., Thakur, S., Singh, S., Dubey, A. K., & Mallik, R. (2016). Dynein Clusters into Lipid Microdomains on Phagosomes to Drive Rapid Transport toward Lysosomes. *Cell*, *164*(4), 722-734. https://doi.org/10.1016/j.cell.2015.12.054

Rai, A. K., Rai, A., Ramaiya, A. J., Jha, R., & Mallik, R. (2013). Molecular adaptations allow dynein to generate large collective forces inside cells. *Cell*, *152*(1-2), 172-182. https://doi.org/10.1016/j.cell.2012.11.044

Rao, L., & Gennerich, A. (2022). Single-Molecule Studies on the Motion and Force Generation of the Kinesin-3 Motor KIF1A. *Methods Mol Biol*, *2478*, 585-608. https://doi.org/10.1007/978-1-0716-2229-2_21

Reck-Peterson, S. L., Redwine, W. B., Vale, R. D., & Carter, A. P. (2018). The cytoplasmic dynein transport machinery and its many cargoes. *Nat Rev Mol Cell Biol*, *19*(6), 382-398. https://doi.org/10.1038/s41580-018-0004-3

Reid, E., Kloos, M., Ashley-Koch, A., Hughes, L., Bevan, S., Svenson, I. K., Graham, F. L., Gaskell, P. C., Dearlove, A., Pericak-Vance, M. A., Rubinsztein, D. C., & Marchuk, D. A. (2002). A kinesin heavy chain (KIF5A) mutation in hereditary spastic paraplegia (SPG10). *Am J Hum Genet*, *71*(5), 1189-1194. https://doi.org/10.1086/344210

Ruhnow, F., Zwicker, D., & Diez, S. (2011). Tracking single particles and elongated filaments with nanometer precision. *Biophys J*, *100*(11), 2820-2828. https://doi.org/10.1016/j.bpj.2011.04.023

Sanghavi, P., Kumar, P., Roy, A., Madhusudhan, M. S., & Mallik, R. (2021). On and off controls within dynein-dynactin on native cargoes. *Proc Natl Acad Sci U S A*, *118*(23). https://doi.org/10.1073/pnas.2103383118

Schroeder, H. W., 3rd, Hendricks, A. G., Ikeda, K., Shuman, H., Rodionov, V., Ikebe, M., Goldman, Y. E., & Holzbaur, E. L. (2012). Force-dependent detachment of kinesin-2 biases track switching at cytoskeletal filament intersections. *Biophys J*, *103*(1), 48-58. https://doi.org/10.1016/j.bpj.2012.05.037

Shukla, S., Troitskaia, A., Swarna, N., Maity, B. K., Tjioe, M., Bookwalter, C. S., Trybus, K. M., Chemla, Y. R., & Selvin, P. R. (2022). High-throughput force measurement of individual kinesin-1 motors during multi-motor transport. *Nanoscale*, *14*(34), 12463-12475. https://doi.org/10.1039/d2nr01701f

Siddiqui, N., Roth, D., Toleikis, A., Zwetsloot, A. J., Cross, R. A., & Straube, A. (2022). Force generation of KIF1C is impaired by pathogenic mutations. *Curr Biol*, *32*(17), 3862-3870 e3866. https://doi.org/10.1016/j.cub.2022.07.029

Soppina, P., Patel, N., Shewale, D. J., Rai, A., Sivaramakrishnan, S., Naik, P. K., & Soppina, V. (2022). Kinesin-3 motors are fine-tuned at the molecular level to endow distinct mechanical outputs. *BMC Biol*, *20*(1), 177. https://doi.org/10.1186/s12915-022-01370-8

Soppina, V., Norris, S. R., Dizaji, A. S., Kortus, M., Veatch, S., Peckham, M., & Verhey, K. J. (2014). Dimerization of mammalian kinesin-3 motors results in superprocessive motion. *Proc Natl Acad Sci U S A*, *111*(15), 5562-5567. https://doi.org/10.1073/pnas.1400759111

Soppina, V., Rai, A. K., Ramaiya, A. J., Barak, P., & Mallik, R. (2009). Tug-of-war between dissimilar teams of microtubule motors regulates transport and fission of endosomes. *Proc Natl Acad Sci U S A*, *106*(46), 19381-19386. https://doi.org/10.1073/pnas.0906524106

Soppina, V., & Verhey, K. J. (2014). The family-specific K-loop influences the microtubule on-rate but not the superprocessivity of kinesin-3 motors. *Mol Biol Cell*, *25*(14), 2161-2170. https://doi.org/10.1091/mbc.E14-01-0696

Sudhakar, S., Abdosamadi, M. K., Jachowski, T. J., Bugiel, M., Jannasch, A., & Schaffer, E. (2021). Germanium nanospheres for ultraresolution picotensiometry of kinesin motors. *Science*, *371*(6530). https://doi.org/10.1126/science.abd9944

Svoboda, K., & Block, S. M. (1994). Force and velocity measured for single kinesin molecules. *Cell*, *77*(5), 773-784. https://doi.org/10.1016/0092-8674(94)90060-4

Thomas, W. E., Trintchina, E., Forero, M., Vogel, V., & Sokurenko, E. V. (2002). Bacterial adhesion to target cells enhanced by shear force. *Cell*, *109*(7), 913-923. https://doi.org/10.1016/s0092-8674(02)00796-1

Thomas, W. E., Vogel, V., & Sokurenko, E. (2008). Biophysics of catch bonds. *Annu Rev Biophys*, *37*, 399-416. https://doi.org/10.1146/annurev.biophys.37.032807.125804

Toleikis, A., Carter, N. J., & Cross, R. A. (2020). Backstepping Mechanism of Kinesin-1. *Biophys J*, *119*(10), 1984-1994. https://doi.org/10.1016/j.bpj.2020.09.034

Tomishige, M., Klopfenstein, D. R., & Vale, R. D. (2002). Conversion of Unc104/KIF1A kinesin into a processive motor after dimerization. *Science*, *297*(5590), 2263-2267. https://doi.org/10.1126/science.1073386

Urbanska, M., Ludecke, A., Walter, W. J., van Oijen, A. M., Duderstadt, K. E., & Diez, S. (2021). Highly-Parallel Microfluidics-Based Force Spectroscopy on Single Cytoskeletal Motors. *Small*, *17*(18), e2007388. https://doi.org/10.1002/smll.202007388

Visscher, K., Schnitzer, M. J., & Block, S. M. (1999). Single kinesin molecules studied with a molecular force clamp. *Nature*, *400*(6740), 184-189. https://doi.org/10.1038/22146

Welte, M. A. (2004). Bidirectional transport along microtubules. *Curr Biol*, *14*(13), R525-537. https://doi.org/10.1016/j.cub.2004.06.045

Woody, M. S., Lewis, J. H., Greenberg, M. J., Goldman, Y. E., & Ostap, E. M. (2016). MEMLET: An Easy-to-Use Tool for Data Fitting and Model Comparison Using Maximum-Likelihood Estimation. *Biophys J*, *111*(2), 273-282. https://doi.org/10.1016/j.bpj.2016.06.019

Yildiz, A. (2025). Mechanism and regulation of kinesin motors. *Nat Rev Mol Cell Biol*, *26*(2), 86-103. https://doi.org/10.1038/s41580-024-00780-6

Yildiz, A., Tomishige, M., Gennerich, A., & Vale, R. D. (2008). Intramolecular strain coordinates kinesin stepping behavior along microtubules. *Cell*, *134*(6), 1030-1041. https://doi.org/10.1016/j.cell.2008.07.018

Zaniewski, T. M., Gicking, A. M., Fricks, J., & Hancock, W. O. (2020). A kinetic dissection of the fast and superprocessive kinesin-3 KIF1A reveals a predominant one-head-bound state during its chemomechanical cycle. *J Biol Chem*, *295*(52), 17889-17903. https://doi.org/10.1074/jbc.RA120.014961

Zaniewski, T. M., & Hancock, W. O. (2023). Positive charge in the K-loop of the kinesin-3 motor KIF1A regulates superprocessivity by enhancing microtubule affinity in the one-head-bound state. *J Biol Chem*, *299*(2), 102818. https://doi.org/10.1016/j.jbc.2022.102818

Zhou, Y., Xu, M. F., Chen, J., Zhang, J. L., Wang, X. Y., Huang, M. H., Wei, Y. L., & She, Z. Y. (2024). Loss-of-function of kinesin-5 KIF11 causes microcephaly, chorioretinopathy, and developmental disorders through chromosome instability

and cell cycle arrest. *Exp Cell Res*, *436*(1), 113975.
https://doi.org/10.1016/j.yexcr.2024.113975

Supporting Information for

DNA tensiometer reveals catch-bond detachment kinetics of kinesin-1, -2 and -3

Crystal R. Noell, Tzu-Chen Ma, Rui Jiang, Scott McKinley, William O. Hancock*

* Corresponding author.
Email: woh1@psu.edu

Supplementary Methods

Biotinylated MT

Tubulin was purified from bovine brain as previously described (Cleary et al., 2022; Uppalapati M, 2009), with the following modifications. After the 45 minute growth phase a 12-fold excess of EZ-link NHS-biotin (Thermo Fisher 20217) was added and incubation at 37℃ continued for another 30 minutes. Microtubules were then depolymerized, polymerized, and pelleted twice to obtain pure biotinylated tubulin. Tubulin concentration was measured by absorbance, and the fraction biotinylated measured using the Biocytin Kit (Thermo Fisher 28022).

Motor Expression, Purification and Oligo Conjugation

Drosophila melanogaster Kinesin-1-EGFP-SNAP-His_6 (aa 1-406) was expressed in Tuner (DE3) E.coli (Addgene #129764). Cells were grown in Terrific Broth (Sigma Aldrich) at 37℃ with shaking at 180 rpm for 4-6 hours until an OD of greater than 1 was reached, then induced with 120 mg IPTG and shaken overnight at 21℃. Cells were harvested the next day, pelleted, resuspended with 1x PBS, frozen, and stored at -80℃. *Rattus norvegicus* Kif1A (aa 1-351)-Kif1A neck linker (NL) (17aa)-Kinesin1 coiled-coil (aa 345-406)-EGFP-SNAP was expressed in Tuner (DE3) E.coli similarly to kinesin-1 (Addgene #229851). *Mus musculus* Kif3A (aa 1-342)-Kif3A NL (17aa)-Kinesin1 coiled-coil (aa 345-406)-EGFP-SNAP was expressed in BL21(DE3) E.coli (Addgene # 229852). Kif1A and Kif3A constructs were synthesized into the kinesin-1 construct backbone by GenScript. His_6 tagged GBP-SNAP in pet28a was also expressed and purified similarly (Feng et al., 2020; Feng et al., 2018; Gicking et al., 2022; Kubala et al., 2010).

Bacterial cell pellets (from 800 mL culture) were thawed and motors were purified via Ni affinity chromatography as described previously (Gicking et al., 2022; Gicking et al., 2019; Zaniewski et al., 2020). Motor proteins were eluted in a buffer containing 20 mM phosphate buffer, 500 mM sodium chloride, 500 mM imidazole, 10 μM ATP and 5 mM DTT. The concentration of pre-labeled motors was then measured by absorbance at 488 nm (using the EGFP extinction coefficient 55,900 $M^{-1}cm^{-1}$), and proteins were visualized with SDS PAGE.

Amine-terminated oligonucleotides (IDT) were resuspended and desalted into 200 mM sodium borate buffer, and the concentration measured by absorbance. The desalted oligo was then mixed with 20-fold excess of BG-GLA-NHS (NEB S9151S, dissolved in DMSO) in 100 mM sodium borate and 50% DMSO and incubated at RT for 30 min. The mixture was then desalted into 1x PBS buffer (containing 1 mM DTT and 1 mM $MgCl_2$). The elution profile was measured by absorbance and the fractions of BG-oligo were pooled. The pre- and post- labeled oligos were visualized on a 10% TBE-Urea gel and stained with SYBR green I. Excess BG-oligo was stored at -20℃.

Immediately following Ni column purification of motors, BG-oligo was mixed with the eluted motor at a 5:1 ratio and incubated on ice for 1 hr. The mixture was then diluted with 1x PBS + 1 mM $MgCl_2$ sufficient to reduce the imidazole concentration to below 80 mM, and a second Ni-affinity purification was carried out to remove the excess BG-oligo. The protein was eluted in the same elution buffer and flash frozen in liquid N_2 in the presence of 10 μM MgATP, 1 mM DTT and 10% sucrose. Final protein

concentration was measured by EGFP absorbance. SDS-PAGE and native PAGE were used to estimate the percentage of motors that have an oligo conjugated to them, typically ~50% were labeled. Oligo-labeled motors were kept at -80℃ for up to a year.

Qdot Labeling

For labelling GFP motors, Qdots were functionalized with GFP-binding protein (GBP) as follows. QDot® ITKTM Amino (PEG) quantum dots (Thermo Fisher Q21541MP) were buffer exchanged by transferring 250uL into a 100K ultrafiltration unit and adding 1x PBS pH 7.4 to make up the filter volume of 4 mL. The sample was centrifuged to the original volume of 250 μL before more buffer was added and the process was repeated 3x. The Qdots were then transferred to a glass vial, BG-GLA-NHS was added in 50-fold excess in a 100 mM sodium borate buffer containing 50% DMSO (v/v), and the reaction incubated for 1 hr at room temperature on a rotator. Excess BG-GLA-NHS was removed by carrying out 5 complete buffer exchanges with a 100K centrifugal concentrating filter. The concentration of BG-Qdots was determined on a plate reader based on a calibration curve from the initial Qdot stock. BG-Qdots were then mixed with GBP-SNAP at a 1:50 ratio and incubated on ice for 1 hour. Qdot-GBP was stored at 4℃ for up to 6 months. On the day of an experiment, Qdot-GBP was mixed with GFP labeled motors at a 10:1 ratio to prevent multi-motor Qdots and incubated on ice for at least 15 minutes before visualization by TIRF.

Geometry Calculations

The maximum theoretical vertical forces in the DNA tensiometer are calculated as follows. The quantum dot does not affect the vertical forces because it is attached to the GFP on the kinesin independent of the attachment to the DNA tether. The kinesin head is ~5 nm (Kull et al., 1996) and the kinesin neck-coil (residue 345-392 at 0.15 nm /residue) is ~7 nm. Assuming that the entire neck-coil is sticking up, the DNA tether starts ~12 nm above the microtubule surface. If the motor and the ~5 nm neutravidin (Rosano et al., 1999) are on the same side of the microtubule, then there is a 7 nm difference relative to the 960 nm extension of the DNA (0.3 deg angle), meaning vertical forces are < 1% of horizontal forces. However, there is evidence that the neck-coil lays parallel to the microtubule (Martin et al., 2010), and so this difference is likely smaller than this. If the motor and the neutravidin are on opposite sides of the microtubule, then the vertical force component (12 nm motor + 5 nm neutravidin + 25 nm Mt; 2.5° angle) will be <5 % of horizontal; however, the direction of load will be pointing into the microtubule surface (and oriented laterally) rather than oriented away from the microtubule. Thus, the geometry is nearly optimal to minimize any upward vertical forces on the motor.

Fitting Equations

Data in Figures 2, S5 and S6 were fit using MEMLET (Woody et al., 2016) to the following single exponential function:

$$\boldsymbol{y(t) = \frac{ke^{-kt}}{e^{-kt_{min}}}}$$

where *k* is the rate constant (inverse of the time constant) and t_{min} is the minimum cutoff of the distribution.

Data in Figure S4 were fit using MEMLET to the following bi-exponential function:

$$\boldsymbol{y(t) = \frac{\left(Ak_1e^{-k_1t} + (1-A)k_2e^{-k_2t}\right)}{(Ae^{-k_1t_{min}}) + \left((1-A)e^{-k_2t_{min}}\right)}}$$

Here A is the amplitude of the first phase, k_1 and k_2 are the rate constants (inverse time constants) of the two phases, and t_{min} is the minimum cutoff of the distribution. This approach corrects the amplitudes for missed events, which can differ for the two phases Cumulative distribution data in Figure 4 were fit by least squares in Matlab to the bi-exponential function:

$$\boldsymbol{y(t) = A_1\left(1 - e^{-\frac{(x-t_0)}{\tau_1}}\right) + (1-A_1)\left(1 - e^{-\frac{(x-t_0)}{\tau_2}}\right)}$$

Here $\boldsymbol{\tau_1}$ and $\boldsymbol{\tau_2}$ are time constants (inverse rate constants) of the two phases, A_1 is the amplitude of the first phase, and t_0 is the minimum cutoff time of the distribution. Amplitudes are normalized to account for missed short events as follows:

$$\boldsymbol{A_{1_{corrected}} = A_1e^{\frac{t_0}{\tau_1}}}$$

$$\boldsymbol{A_{2_{corrected}} = (1-A_1)e^{\frac{t_0}{\tau_2}}}$$

$$\boldsymbol{A_{1_{corrected_{relative}}} = \frac{A_{1_{corrected}}}{A_{1_{corrected}} + A_{2_{corrected}}}}$$

$$\boldsymbol{A_{2_{corrected_{relative}}} = \frac{A_{2_{corrected}}}{A_{1_{corrected}} + A_{2_{corrected}}}}$$

Inference Strategy for Ramp Duration Parameter

The primary challenge in assessing ramp runs is that these segments can end for one of two reasons: either (1) the motor detaches, or (2) the motor reaches a distance sufficiently far from the anchor to enter a stalled state. By contrast, unloaded runs and stall segments all end in detachments from microtubules. So, while taking a simple average of segment durations will result in an “average time until detachment” for unloaded and stalled segments, this is not the case for ramps. Moreover, ambiguity as to when a ramp run begins further confirms that a simply average of ramp segment durations will lead to errors. This issue is similar to the one raised in Rayens et al. (Rayens et al., 2022) in which the authors sought to estimate the average stationary segment length for motor-lysosome complexes in vivo, even though the length of some stationary segments exceeded the length of the observation window.

One way to address the problem of truncated durations is to assume that state-switching satisfies the Markov property, which is to say that whether an agent switches

states in a given time step is independent of states and switches that occurred during previous time steps. for continuous time Markov chains, models are expressed in terms of rates, and so the natural quantity of interest here is the detachment rate, which might commonly be denoted k_{off}. Within the text, we wish to compare ramp state properties to unloaded and stall states which are quantified in terms of their average duration. In this note we therefore write the detachment rate in terms of a duration parameter $\tau = 1/k_{\text{off}}$. Generically, the probability that a continuous-time Markov chain does not change state in a segment of time $[a, b]$ is given by the formula:

$$P(\text{No change during } [\text{a}, \text{b}]) = e^{-\int_a^b \kappa(t)dt},$$

where $\kappa(t)$ the (possibly evolving) rate at which changes occur. If we assume that the detachment rate $1/\tau$ is constant, then in any segment of length Δ, the probability that a motor does not detach is

$$P(\text{No change during } [\text{a}, \text{b}]) = e^{-\frac{\Delta}{\tau}},$$

Suppose that $(t_0, t_1, \ldots, t_n)$ are observation times of a tensiometer run and let T denote the time that a motor would detach were it not for transitions to stall. Then the probability that a detachment occurs in the interval $[t_k, t_{k+1})$ is product of the probabilities it does not detach in all preceding segments multiplied by the probability it does detach in the final one. This idea is shown in the diagram below. The initial green segments are ramps which may result in a detachment (yellow star), or result in conversion to a stall state (red line) which always ends in a detachment. In describing our approach to inference, we denote the ramp durations $\{T_i\}_{i=1}^{N+M}$ and the stall durations are $\{S_i\}_{i=1}^{M}$. This notation scheme implies that there were N detachment events during ramp segments.

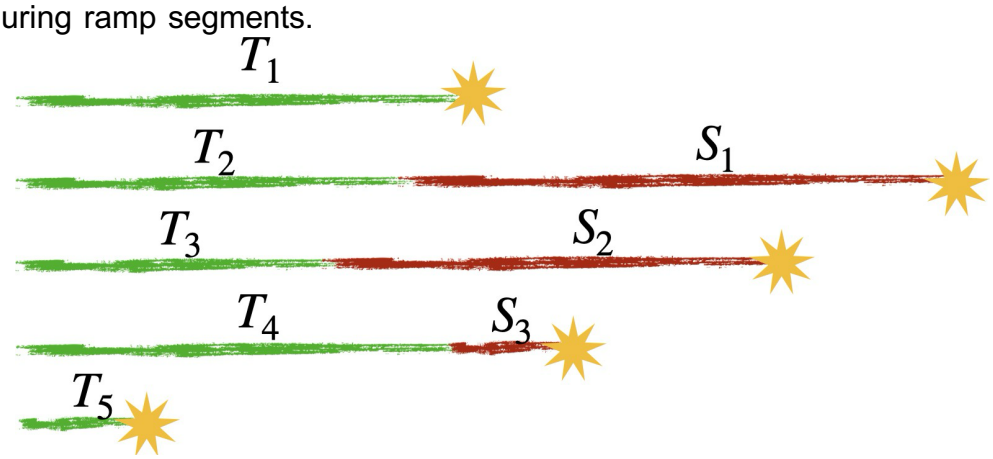

Mathematically, we write

$$P\big(T \in [t_k, t_{k+1})\big) = \Big(\prod_{i=1}^{k} e^{\frac{-(t_i - t_{i-1})}{\tau}}\Big)\left(1 - e^{\frac{-(t_{k+1} - t_k)}{\tau}}\right)$$
$$= e^{-\frac{-(t_k - t_0)}{\tau}}\left(1 - e^{\frac{-(t_{k+1} - t_k)}{\tau}}\right)$$

Assuming that time increments are evenly spaced and of size Δ, and also assuming that Δ is small compared to the duration parameter τ, we can take the first term of the Taylor expansion of the $(t_{k+1} - t_k)$ term and simplify:

Ramp with detachment: $P\big(T \in [t_k, t_{k+1})\big) \approx e^{\frac{-(t_k - t_0)}{\tau}} \frac{\Delta}{\tau}$

On the other hand, suppose that the motor switches to a stalled state after time t_k. Then the initial product of non-detaching segments remains the same, and final term is removed:

Ramp without detachment: $P\big(T \in [t_k, t_{k+1})\big) \approx e^{\frac{-(t_k - t_0)}{\tau}}$

To unify the notation, let 1_i^{det} denote the event that the *i* ramp run detached before reaching stall phase. We have

$$P\big(T \in [t_k, t_{k+1})\big) \approx \left(\frac{\Delta}{\tau}\right)^{1_i^{det}} e^{\frac{-(t_k - t_0)}{\tau}}$$

To perform inference on multiple runs, we assume they are independent and so, again, we can take a simple product. As described in the caption of Figure 1, let $\{T_i\}_{i=1}^{N+M}$ be an enumeration of ramp durations, where *N* is the number of ramps that detached and *M* is the number of ramps that reached a stall state. It follows that the likelihood of observing a set of trajectories *X* given a duration parameter *τ* can be written

$$\begin{aligned} P(X;\tau) &= \prod_{i=1}^{N+M} \left(\frac{\Delta}{\tau}\right)^{1_i^{det}} e^{\frac{-T_i}{\tau}} \\ &= \left(\frac{\Delta}{\tau}\right)^{N} e^{\frac{-\sum T_i}{\tau}} \end{aligned}$$

From a Bayesian perspective, we can use this likelihood function to create a posterior distribution for the duration parameter *τ*. In this work we have used a scale-free uninformative prior (Robert, 1994) of the form $\pi(r) = r^{-1}$. Together with the likelihood, we have that the posterior distribution has the form

$$\begin{aligned} \pi(\tau|X) &\overset{c}{=} P(X;\tau)\pi(\tau) \\ &= \Delta^N \tau^{-(N+1)} e^{\frac{-\sum T_i}{\tau}} \end{aligned}$$

where $\overset{c}{=}$ means "equals up to a constant depending only on *X*". Looking at the factors that depend only on *τ* this is an Inverse Gamma distribution.

In this way, we reach the conclusion that if *T* is the total time spent in the ramp states and if *N* is the number of detachments while in the ramp state, the posterior distribution for the duration parameter is

$$\pi(\tau|T,N) \sim \text{InvGamma}(N, T).$$

This means that it has pdf

$$f(t;N,T) = \frac{T^N}{\Gamma(N)} \frac{1}{t^{\alpha+1}} e^{\frac{-T}{\tau}}$$

and, most importantly for the purpose of estimation, the mean of the posterior distribution is simply *T*/*N*. In other words, the simple Bayes estimator for a collection of ramp segments is:

$$\hat{\tau} = \frac{T}{N} = \frac{\text{Total time in ramp phase}}{\text{Number of detachments in ramp phase}}$$

To set our 100(1 − *α*) %-credible regions, we used the middle-*α* probability range from the posterior distribution. This means that the 95% credible region is defined as the interval between the 0.025-quantile and 0.975-quantile of the posterior distribution. These regions are indicated as solid lines segments beneath the posterior distributions depicted in Figure 3 in the main text.

Compensating for Difficulty in Observing Short Runs

For unloaded and ramp runs there is a significant risk that short runs will be unobserved. For ramp runs, short ramp phases might be masked by the fluctuations that occur when the motor is detached. Meanwhile, short, unloaded runs might not be recognized among many motors in a wide field of view. Among kinesin-1 runs, for example, the shortest recorded unloaded run was 0.48s, despite the frame rate being significantly smaller. The minimum recorded times, t_{min} (seconds), for each category of run observations is as follows:

	Stall	Ramp	Unloaded
Kinesin-1	0.1	0.14	0.48
Kinesin-2	0.22	0.17	0.348
Kinesin-3	0.03	0.03	0.641

The likelihood function therefore needs to be adjusted to be conditioned on being greater than the minimum observation time for that cohort. Continuing with the notation from above (for convenience taking $t_0 = 0$, let T_i denote the ith run duration. Then the joint likelihood function is therefore

$$P(T \in [t_k, t_{k+1}) | T_i > t_{\text{min}}) = \frac{P(T \in [t_k, t_{k+1}), T_i > t_{\text{min}})}{P(T_i > t_{\text{min}})}$$

$$\approx \frac{1_{t_k > t_{\text{min}}} e^{\frac{-t_k}{\tau}} \Delta}{e^{\frac{-t_{\text{min}}}{\tau}}}$$

$$= 1_{t_k > t_{\text{min}}} e^{\frac{-(t_k - t_{\text{min}})}{\tau}} \frac{\Delta}{\tau}$$

For a collection of paths χ, the likelihood function becomes

$$P(X|\tau, t_{\text{min}}) = \prod_{i=1}^{N+M} 1_{T_i > t_{\text{min}}} \left(\frac{\Delta}{\tau}\right)^{1_i^{det}} e^{\frac{-(T_i - t_\text{min})}{\tau}}$$

$$= 1_{\min_i T_i > t_{\text{min}}} \left(\frac{\Delta}{\tau}\right)^{N} e^{\frac{-(T_i - t_\text{min})}{\tau}}$$

Note that for any fixed value τ, the maximum of the likelihood function over all t_{min} values is $t_{\text{min}} = \min_i T_i$. Rather than constructing a joint Bayesian posterior for the pair (τ, t_{min}), we simply adopted the maximum likelihood value for t_{min} within each cohort and proceeded as described above with the likelihood function

$$P(X; \tau) \left(\frac{\Delta}{\tau}\right)^{N} e^{\frac{-\sum_i (T_i - \min_j T_j)}{\tau}}$$

Rate Constant Constraints in Stochastic Model

To constrain the rate constants in the stochastic model simulations using the experimental results, the model was solved analytically, as follows. The forward stepping rate and the load-dependent velocity are:

$$k_{forward} = \left(\frac{1}{k_{S-W}} + \frac{1}{k_{W-S}}\right)^{-1}$$

$$V(F) = 8\,nm * (k_{forward} - k_{back})$$

Ignoring relatively slow backstepping rate of 3 s^{-1} in the stepping cycle, the bound duration is equal to the duration of each step multiplied by the predicted number of steps before detaching:

$$T(F) = \left(\frac{1}{k_{S-W}} + \frac{1}{k_{W-S}}\right)^{-1} * \left(\frac{k_{W-S} + k_{slip}}{k_{W-S}}\right)$$

The forward stepping rates for unloaded kinesin-1, -2, -3 simulations were set based on the unloaded velocities to 84.5, 53 and 151.5 steps per second, respectively. At stall, defined as a force of 6 pN, the forward stepping rates were set to 3 s^{-1}, matching the backstepping rate. The transition to the slip state, k_{slip}, was chosen based on the run and stall durations for each motor.

To simulate restarting times, the rate constants were constrained by the restart time constants (τ) and respective weights (A) in Figure 4. The rescue rate (k_{resc}) and two slip-to-detached transition rates (k_{det1}& k_{det2}) were determined based on the shortest time constant (τ_1) as follows,

$$\tau_1 = \frac{1}{k_{resc} + k_{det1} + k_{det2}}$$

$$k_{resc} = A_{\tau_1} * \frac{1}{\tau_1}$$

$$k_{det1} = A_{\tau_2} * \frac{1}{\tau_1}$$

$$k_{det2} = A_{\tau_3} * \frac{1}{\tau_1}$$

This formulation accounted for the relative amplitudes of the three time constants. The reattachment rates (k_{reatt1} & k_{reatt2}) were defined based on the two slower restart time constants by considering that the time to restart is the sum of time spent in the slip state plus the time spent in the detached state. The two reattachment rates were defined as follows,

$$\tau_2 = \tau_1 + \frac{1}{k_{reatt1}}$$

$$\tau_3 = \tau_1 + \frac{1}{k_{reatt2}}$$

This process was repeated for the three motor families.

Table S1. Predicted force imposed on the motor during the ramp phase

	$v_{unloaded}$ (nm/s)	v_{ramp} (nm/s)	v_{ramp} / $v_{unloaded}$	$F_{predicted}$ (pN)*
Kinesin-1	651	572	0.88	0.72
Kinesin-2	401	324	0.81	1.14
Kinesin-3	1458	1187	0.81	1.14

*Based on linear force-velocity relationship with a 6 pN stall force

Table S1. Fit results for unloaded, ramp, and stall durations

		Results from a Maximum Likelihood Estimator (MEMLET) (Fig. 2)		Results from Markov model coupled with Bayesian inference (Fig. 3)	
Motor	**State**	**τ (s)**	**95% CI (s)**	**τ (s)**	**95% CI (s)**
Kinesin-1	Unloaded	1.04	0.79 – 1.30	1.05	0.81 – 1.36
	Ramp			2.49	1.87 – 3.32
	Stall	3.01	2.30 – 3.79	3.05	2.43 – 3.83
Kinesin-2	Unloaded	1.07	0.85 – 1.35	1.09	0.88 – 1.34
	Ramp			0.97	0.87 – 1.08
	Stall	2.83	2.03 – 3.79	2.90	2.17 – 3.86
Kinesin-3	Unloaded	2.74	2.33 – 3.17	2.76	2.28 – 3.34
	Ramp			0.75	0.64 – 0.87
	Stall	1.89	1.53 – 2.31	1.90	1.60 – 2.25

Table S3: Reattachment Statistics

Reattachment Tri-Exponential Statistics						
	τ_1 (s)	A_1	τ_2 (s)	A_2	τ_3 (s)	A_3
Kinesin-1	0.04 [0.03, 0.04]	0.51 [0.34,0.74]	1.50 [1.35,1.65]	0.46 [0.38, 0.58]	20.5 [0.00, 61.13]	0.03 [0.00, 0.07]
Kinesin-2	0.13 [0.11, 0.16]	0.42 [0.00, 1.00]	0.91 [0.45, 1.00]	0.45 [0.14, 1.00]	3.65 [0.00, 8.61]	0.13 [0.00, 1.00]
Kinesin-3	0.03 [0.02, 0.03]	0.53 [0.32, 0.84]	0.15 [0.09, 0.21]	0.16 [0.11, 0.25]	1.35 [1.24, 1.44]	0.31 [0.24, 0.41]

*95% Confidence intervals determined by bootstrapping with 1000 iterations are indicated in brackets

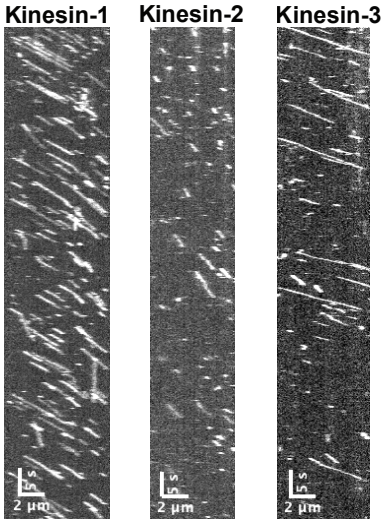

Figure. S1. Kymographs of unloaded GFP-labeled kinesins. GPF-labeled motors conjugated to their complimentary oligo were visualized via TIRF at a concentration of 1 nM at 5 fps. No neutravidin, Qdot or DNA are present in these unloaded controls. Of note, a portion of kinesin-3 unloaded run durations were limited by the length of the microtubules, meaning the unloaded duration is a lower limit.

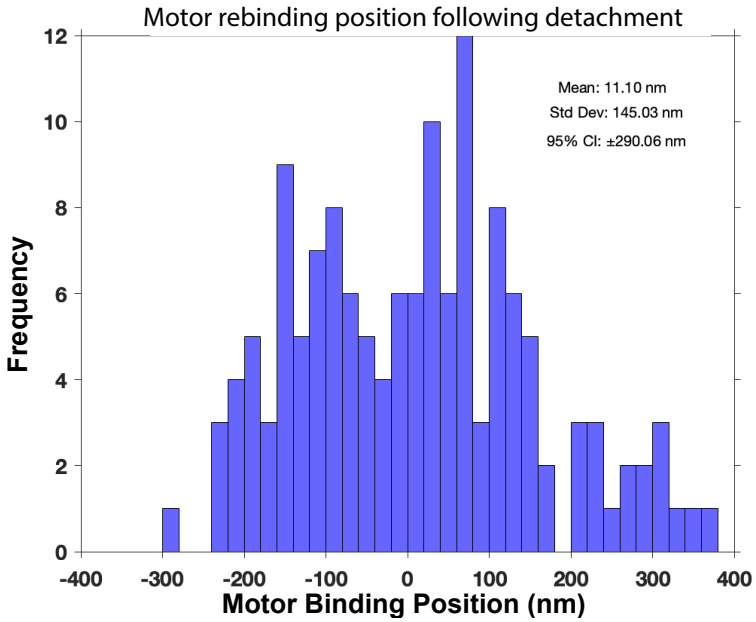

Figure. S2. Distribution of initial motor binding positions. The initial positions were measured for events where the motor was clearly dissociated from the microtubule and fluctuated around origin on its DNA tether (N=141). The zero position was determined as the center point around which the detached motor fluctuated. The initial motor binding position was determined by the first start point of a ramp. The width of the gaussian distribution, quantified by the SD, demonstrates the large search space of the motor attached to the flexible ~1-micron dsDNA tether. The mean of +11 nm likely results from some of the motors moving before the first frame acquisition, giving a small positive bias. The larger population seen at >+200 nm relative to <-200 nm may result from dissociation of motors that bind under assisting loads (negative displacements) and strengthening of motors that bind under hindering loads (positive displacements). Data are from kinesin-1 and kinesin-3 tensiometers.

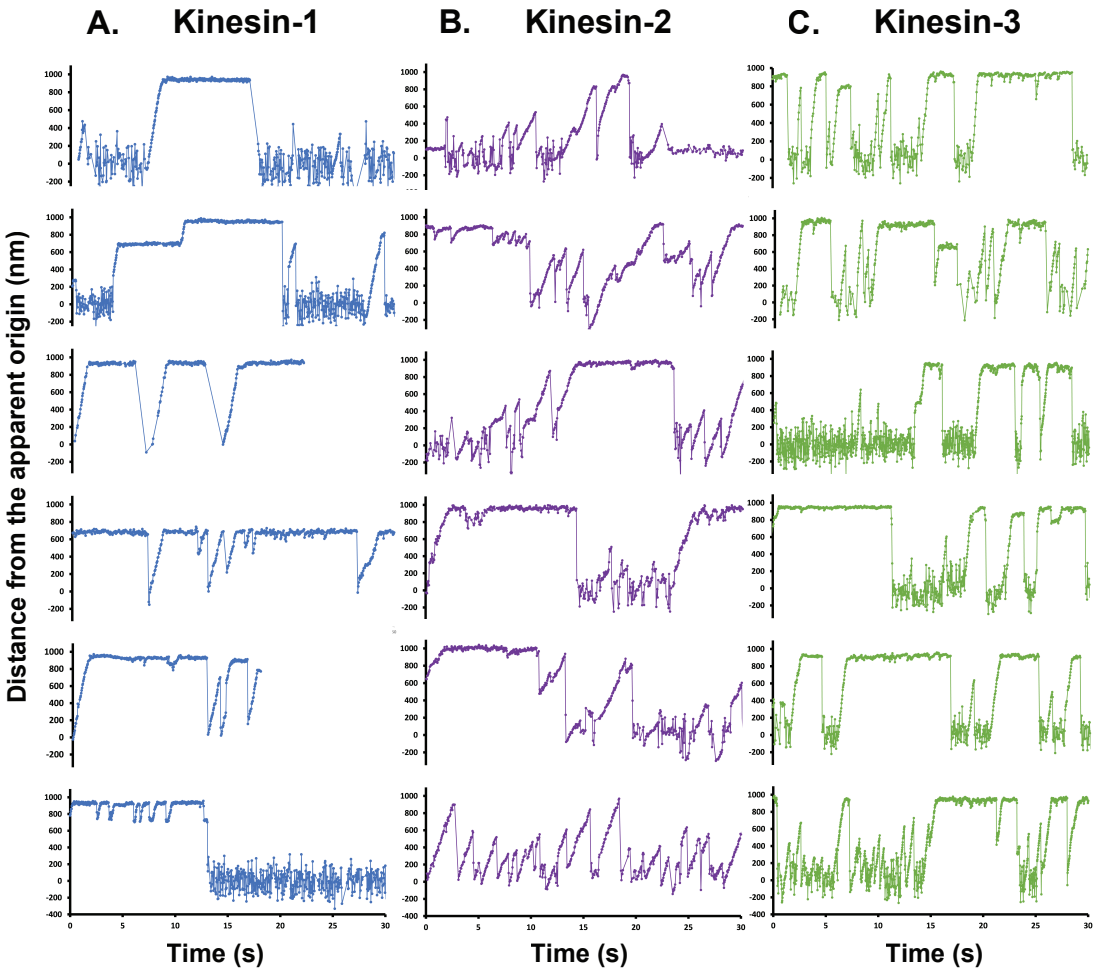

Figure S3. Further kinesin tensiometer examples. Distance versus time plots of (A) kinesin-1, (B) kinesin-2 and (C) kinesin-3 traces. Notably, some stalls are very stable, whereas other (particularly for kinesin-2 and kinesin-3) show fluctuations, presumably due to small slips and backstepping at stall. Other features to note include pauses in the motile segments, small changes in velocity, and repeated ramps for kinesin-2. Roughly 20% of tensiometers extended less than the expected 1 μm distance, stalling repeatedly at 500 nm or 800 nm. These apparently shorter DNA strands may result from DNA secondary structures or from primer binding at a secondary sequence. After in-depth comparison of the data we found that the stall durations, reattachment rates, and starting positions were unaffected by the shorter DNA length and thus included the shorter tensiometers in our data set.

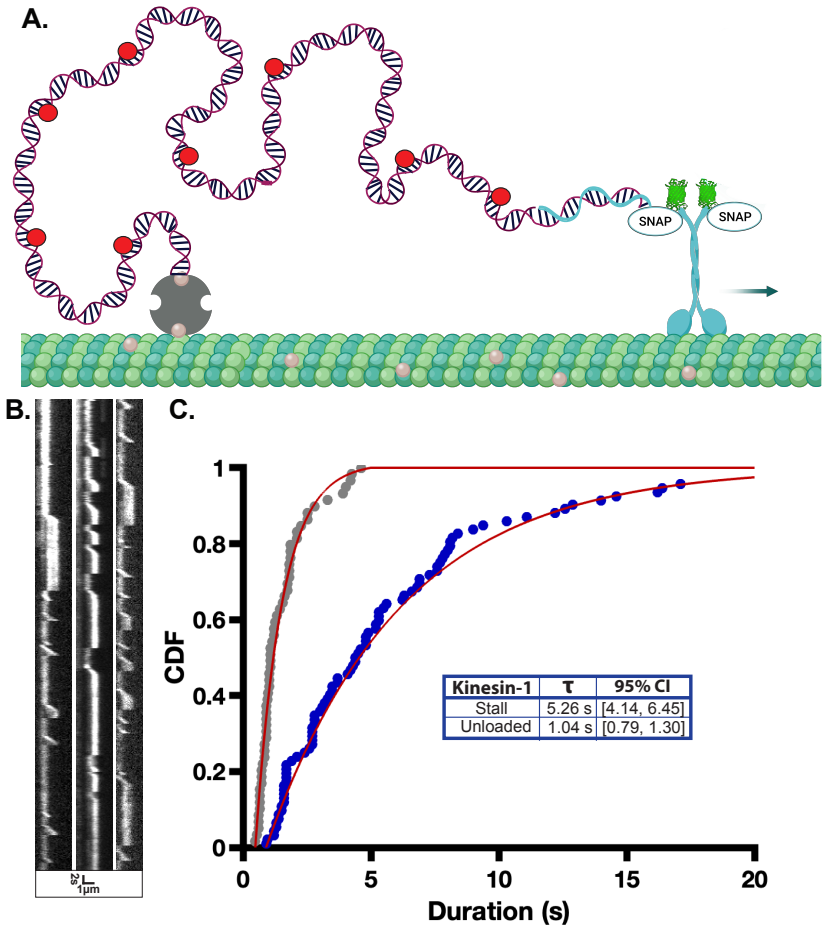

Figure S4. Long stall durations are observed in the absence of Qdots. Because the Qdots used in our experiments are functionalized with multiple GBP nanobodies, there is the possibility that the long stall durations observed were caused by multiple motors bound to the Qdots. To test this, we ran a control experiment where, instead of labeling the motors with Qdots, we fluorescently labeled our dsDNA by incorporating 5% dCTP-Cy5 during the PCR reaction to create fluorescent dsDNA. By removing Qdots from the system, the potential for multimotor events is eliminated. (A) Diagram of control experiment. (B) TIRF kymographs of representative bright kinesin-1 DNA tensiometers collected at 5 fps, showing the typical extension and stall profiles we observed in Figure 1, with the difference that the entire dsDNA is visualized rather than the Qdot. (C) CDF plot of the fluorescent DNA tensiometer stall durations of kinesin-1, fit with a single exponential function using a maximum likelihood estimator (MEMLET). Importantly, kinesin-1 continued to have much longer stall durations than its unloaded run durations (gray points with fit; reproduced from Fig. 2A), ruling out multi-motor interactions as the cause of the long stall durations. The longer stall durations here (5.26 s) compared to the Qdot stall durations (3.01 s; Fig. 2A) is attributed to the 5 fps frame rate used in here, which makes it more difficult to detect short slip events that are observed with the 25 fps Qdot movies.

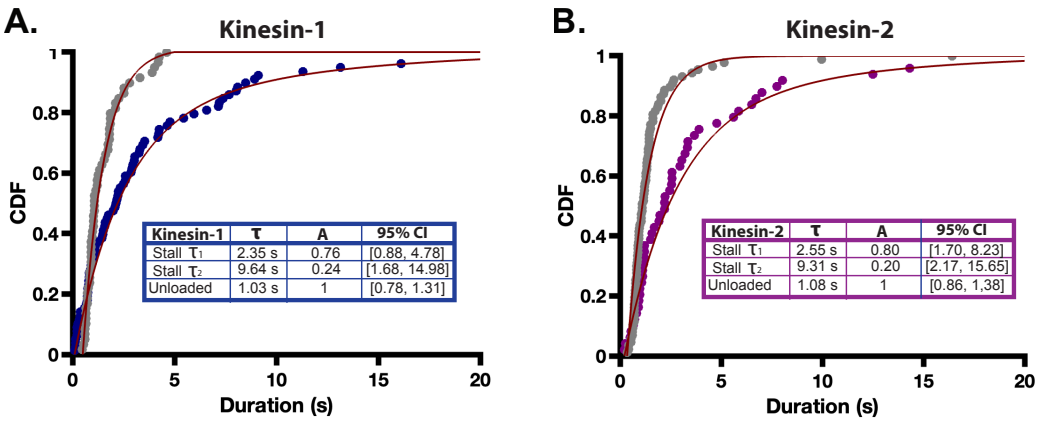

Kinesin-1	τ	A	95% CI
Stall τ_1	2.35 s	0.76	[0.88, 4.78]
Stall τ_2	9.64 s	0.24	[1.68, 14.98]
Unloaded	1.03 s	1	[0.78, 1.31]

Kinesin-2	τ	A	95% CI
Stall τ_1	2.55 s	0.80	[1.70, 8.23]
Stall τ_2	9.31 s	0.20	[2.17, 15.65]
Unloaded	1.08 s	1	[0.86, 1,38]

Figure S5. Bi-exponential fits of stall durations reveal a longer duration sub-population for kinesin-1 and kinesin-2. Tensiometer stall durations of (A) kinesin-1 and (B) kinesin-2 were fit with a biexponential function using a maximum likelihood estimator, MEMLET (https://michaelswoody.github.io/MEMLET/). Unloaded run durations are shown in gray for reference. Time constants (τ), relative amplitudes (A) and 95% confidence intervals for time constants are given in the accompanying tables. The rationale for why the motors would have two time constants is not clear, but it may suggest two alternative detachment pathways. Notably, both time constants are longer than the unloaded binding duration for both motors. Kinesin-3 stall durations were well fit by a single exponential function (see Fig. 2C).

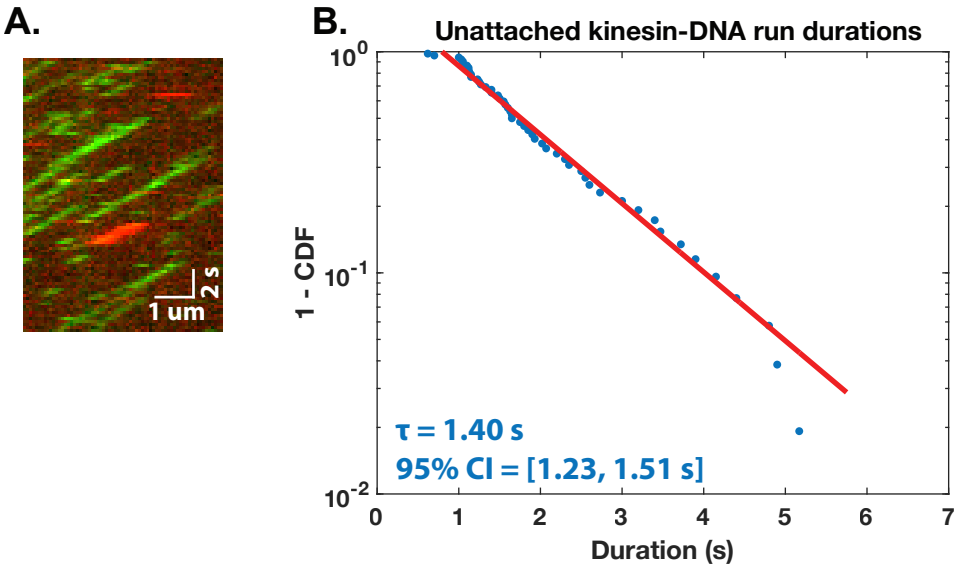

Figure S6. Unloaded run durations of kinesin-DNA complexes not bound through biotin-streptavidin to the microtubule. GFP-labeled kinesin-1 conjugated to its complimentary oligo was incubated with the 3kb Cy5-labeled dsDNA for several hours and then visualized via TIRF microscopy on unlabeled microtubules, videos were recorded at 5fps. (A) Kymograph shows free kinesin-1 motors (green) and kinesin-DNA complexes (red). (B) The kinesin-DNA run times (N=52) were measured by kymograph analysis in ImageJ and fit to a single exponential using least squares, with t_0 minimum cutoff of 0.79 s. 95% CI was determined via bootstrapping with 1000 iterations.

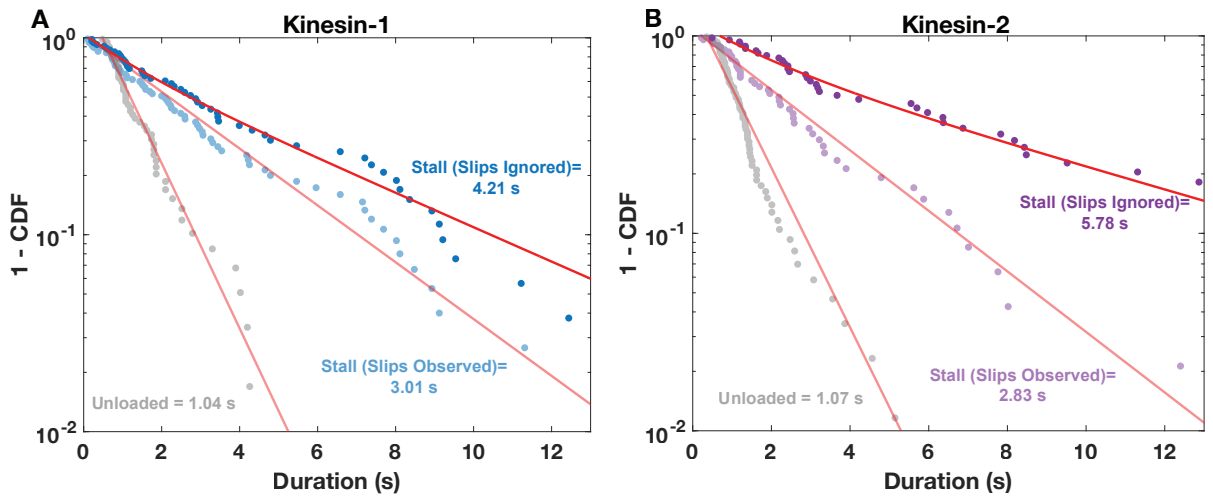

Figure S7. Stall durations are longer when slips are ignored. (A) Kinesin-1 stall durations, with unloaded run times in gray, stall durations terminated by slips in light blue, and stall durations terminated by falling to the baseline (ignoring slips) in dark blue. Unloaded and stall durations (from Figure 2) were fit with single exponential functions in MEMLET. Stall durations ignoring slips were fit with a bi-exponential by least squares τ_1 = 1.35 s [95% CI: 0.81, 1.91 s], A_1 = 0.27 s [0.07, 0.62 s], τ_2 = 4.99 s [4.45, 5.93], A_2 = 0.77 [0.46, 1.00]. Weighted average of the two time constants is displayed in plot for comparison to other time constants. (B) Kinesin-2 is plotted similarly in purple, fitting of stall duration ignoring slips resulted in τ_1 = 1.91 s [95% CI: 0.92, 2.78 s], A_1 = 0.32 s [0.11, 0.79 s], τ_2 = 7.60 s [6.74, 9.05], A_2 = 0.68 [0.41, 1.00].

A

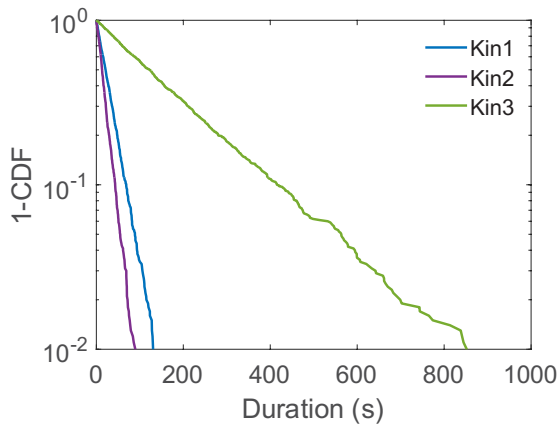

B

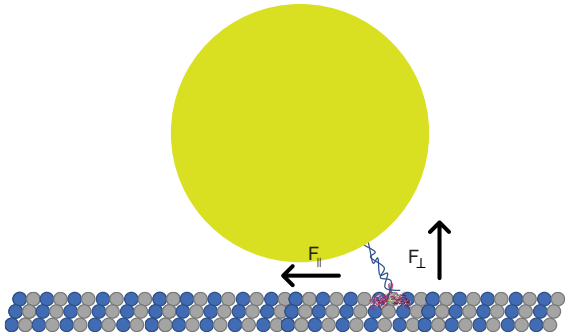

C

Kinesin -1	Unloaded duration (s)	Stall duration (s)
One-bead experiment[1]	0.9	0.37
Model with $F_\parallel$&$F_\perp$ [2]	1.1	0.34
Khataee model with $F_\parallel$&$F_\perp$ [3]	1.2	0.34
DNA-tensiometer[4]	1.0	3.0
Model with $F_\parallel$ only[5]	1.1	2.9
Khataee model with $F_\parallel$ only[6]	1.2	77

Figure S8: Model results incorporating both vertical and horizontal forces.
(A) Model results incorporating load-dependent $k_{S\text{-}W}$ and load-independent k_{slip}. Very long stall durations are predicted that don't agree with results, which motivated incorporating a load-dependence into k_{slip} (Figure 5). (B) Diagram of single-bead optical tweezer experiment using 440 nm diameter bead and 35 nm long motor, which results in a 60° motor angle. With this geometry, a 6 pN stall force parallel to the microtubule is associated with a 10 pN vertical force on the motor. Note that figure is not to scale. (C) Evaluation of effects of vertical and horizontal load from different models. [1]One-bead experimental data at zero and 6 pN from Andreasson (Andreasson et al., 2015; Khataee & Howard, 2019) [2]Our model incorporating both horizontal and vertical forces into k_{slip} (using $\delta_\parallel$ = 1.61 nm and $\delta_\perp$ = 1.58 nm) is able to match the single-bead stall duration. [3]Khataee model (Khataee & Howard, 2019) also accounts for single-bead unloaded and stall durations. [4]Kinesin-1 DNA tensiometer data. [5]When modeling our DNA tensiometer data for kinesin-1, our model using only $F_\parallel$ is able to match the stall duration, whereas the Khataee model[6] overestimates the stall duration.

SI References

Andreasson, J. O., Shastry, S., Hancock, W. O., & Block, S. M. (2015). The Mechanochemical Cycle of Mammalian Kinesin-2 KIF3A/B under Load. *Curr Biol*, *25*(9), 1166-1175. https://doi.org/10.1016/j.cub.2015.03.013

Cleary, J. M., Kim, T., Cook, A. S. I., McCormick, L. A., Hancock, W. O., & Rice, L. M. (2022). Measurements and simulations of microtubule growth imply strong longitudinal interactions and reveal a role for GDP on the elongating end. *Elife*, *11*. https://doi.org/10.7554/eLife.75931

Feng, Q., Gicking, A. M., & Hancock, W. O. (2020). Dynactin p150 promotes processive motility of DDB complexes by minimizing diffusional behavior of dynein. *Mol Biol Cell*, *31*(8), 782-792. https://doi.org/10.1091/mbc.E19-09-0495

Feng, Q., Mickolajczyk, K. J., Chen, G. Y., & Hancock, W. O. (2018). Motor Reattachment Kinetics Play a Dominant Role in Multimotor-Driven Cargo Transport. *Biophys J*, *114*(2), 400-409. https://doi.org/10.1016/j.bpj.2017.11.016

Gicking, A. M., Ma, T. C., Feng, Q., Jiang, R., Badieyan, S., Cianfrocco, M. A., & Hancock, W. O. (2022). Kinesin-1, -2, and -3 motors use family-specific mechanochemical strategies to effectively compete with dynein during bidirectional transport. *Elife*, *11*. https://doi.org/10.7554/eLife.82228

Gicking, A. M., Wang, P., Liu, C., Mickolajczyk, K. J., Guo, L., Hancock, W. O., & Qiu, W. (2019). The Orphan Kinesin PAKRP2 Achieves Processive Motility via a Noncanonical Stepping Mechanism. *Biophys J*, *116*(7), 1270-1281. https://doi.org/10.1016/j.bpj.2019.02.019

Khataee, H., & Howard, J. (2019). Force Generated by Two Kinesin Motors Depends on the Load Direction and Intermolecular Coupling. *Phys Rev Lett*, *122*(18), 188101. https://doi.org/10.1103/PhysRevLett.122.188101

Kubala, M. H., Kovtun, O., Alexandrov, K., & Collins, B. M. (2010). Structural and thermodynamic analysis of the GFP:GFP-nanobody complex. *Protein Sci*, *19*(12), 2389-2401. https://doi.org/10.1002/pro.519

Kull, F. J., Sablin, E. P., Lau, R., Fletterick, R. J., & Vale, R. D. (1996). Crystal structure of the kinesin motor domain reveals a structural similarity to myosin. *Nature*, *380*(6574), 550-555. https://doi.org/10.1038/380550a0

Martin, D. S., Fathi, R., Mitchison, T. J., & Gelles, J. (2010). FRET measurements of kinesin neck orientation reveal a structural basis for processivity and asymmetry. *Proc Natl Acad Sci U S A*, *107*(12), 5453-5458. https://doi.org/10.1073/pnas.0914924107

Rayens, N. T., Cook, K. J., McKinley, S. A., & Payne, C. K. (2022). Transport of lysosomes decreases in the perinuclear region: Insights from changepoint analysis. *Biophys J*, *121*(7), 1205-1218. https://doi.org/10.1016/j.bpj.2022.02.032

Robert, C. P. (1994). *The Bayesian Choice*. Springer.

Rosano, C., Arosio, P., & Bolognesi, M. (1999). The X-ray three-dimensional structure of avidin. *Biomol Eng*, *16*(1-4), 5-12. https://doi.org/10.1016/s1050-3862(99)00047-9

Uppalapati M, H. Y., Shastry S, Jackson TN, Hancock WO. (2009). Methods in Bioengineering: Microfabrication and Microfluidics. In J. DZ (Ed.), (pp. 311-336).

Woody, M. S., Lewis, J. H., Greenberg, M. J., Goldman, Y. E., & Ostap, E. M. (2016). MEMLET: An Easy-to-Use Tool for Data Fitting and Model Comparison Using Maximum-Likelihood Estimation. *Biophys J*, *111*(2), 273-282. https://doi.org/10.1016/j.bpj.2016.06.019

Zaniewski, T. M., Gicking, A. M., Fricks, J., & Hancock, W. O. (2020). A kinetic dissection of the fast and superprocessive kinesin-3 KIF1A reveals a predominant one-head-bound state during its chemomechanical cycle. *J Biol Chem*, *295*(52), 17889-17903. https://doi.org/10.1074/jbc.RA120.014961